A STUDY OF
GROUND PENETRATING RADAR METHODS IN AN UNDERGROUND STONE MINE TO IMPROVE GROUND CONTROL

Jonathan Baggett

Thesis submitted to the faculty of the Virginia Polytechnic Institute and State University in partial fulfillment of the requirements for the degree of

Master of Science

In

Mining Engineering

Nino S. Ripepi, Chair

Erik C. Westman

John A. Hole

May 7, 2019

Blacksburg, VA

Keywords: Ground Penetrating Radar, GPR, Karst Voids, Underground Stone Mines

AN INVESTIGATION OF
GROUND PENETRATING RADAR METHODS IN AN UNDERGROUND STONE MINE
TO IMPROVE GROUND CONTROL

Jonathan Baggett

ACADEMIC ABSTRACT

This work focuses on the operational and safety issues associated with karst voids in large opening underground mines. Issues include water inrush, structural instability, and engineering uncertainty in these environments. Coupled with the fracturing prevalent in folded sedimentary rocks, karsts are complex and challenging ground control risks.

Traditional methods of predicting karst void locations such as probe-drilling are impeded by the inconsistent spatial distribution and variable sizes of the features. Ground penetrating radar (GPR) is a geophysical technique that transmits radio waves into a medium and subsequently detects reflected waves via a receiver. The travel time and energy of received signals are then processed and interpreted. The difference in material properties between limestone and open karst voids causes strong reflections.

This work summarizes a series of 2D and 3D GPR surveys for karst void mapping within a mine pillar and within sill pillars between mine levels in a large opening underground limestone mine. In this case study mine, karst voids are hazardous ground control risks that interact with geologic discontinuities, creating free blocks within the rock mass. As tunnels are advanced via blasting, unknown karst voids may be exposed and pose risks to mining personnel. The karst voids also form a hydrogeological network of water reservoirs with spatial locations throughout the rock mass that are difficult to predict with traditional methods such as drilling.

While GPR has been utilized throughout several industries for anomaly detection, mapping, and validating other geophysical datasets, this technique has not seen the same proliferation within the mining industry. Regarding published literature, there is a lack of works that detail the applicability of GPR in underground mining scenarios. The aim of this work is to expand on previous methodologies establishing GPR as a useful tool in underground mining applications, and to discuss the benefits and limitations GPR data in such scenarios.

AN INVESTIGATION OF
GROUND PENETRATING RADAR METHODS IN AN UNDERGROUND STONE MINE
TO IMPROVE GROUND CONTROL

Jonathan Baggett

GENERAL AUDIENCE ABSTRACT

This work focuses on the operational and safety issues associated with karst voids in large opening underground mines. Typical issues include water flooding into the tunnels and rocks falling out from the roof and walls, among other things. Sedimentary rock structures sometimes are geologically complex, and karst voids only add to that complexity.

Engineers usually predict karst void locations with drilling or statistics, but this is often challenging as karst voids have various shapes and orientations. Ground penetrating radar (GPR) is a geophysical technique that sends electric signals into the rock; these signals can reflect off of karst voids and other anomalies. The travel time and energy of signals that come back to the antennas are then processed and interpreted. The difference in material properties between limestone and open karst voids causes strong reflections.

This work shows a series of 2D and 3D GPR surveys for karst void mapping within a pillar in a stone mine and also below the floor of mine tunnels. In this mine, karst voids are very dangerous and the miners spend significant time and resources to ensure the tunnels walls are stable. As tunnels are blasted, hidden karst voids may be exposed and pose unpredicted risks to miners. The karst voids are also connected by cracks and discontinuities, providing a path for water to travel along.

While GPR has been used in various ways among the construction, civil engineering, and tunneling industries, there is not enough literature pertaining to its benefits for mines. The goal of this work is to grow the available literature on GPR in mining and to talk about the best practices for GPR use as a means of improving health and safety for miners underground

ACKNOWLEDGEMENTS

First, I want to acknowledge my advisor Dr. Nino Ripepi for offering support and guidance throughout both my undergraduate and graduate careers, and for inviting me into the community of researchers who I have worked among and grown with for the past few years. In all sorts of challenging situations, he reminded me that research can be and should an exciting endeavor.

I would like to thank my committee members for their support. In Dr. Hole I found valuable collaboration, had much needed technical discussions, and learned how essential good field notes can be. I also thank Dr. Westman for his professionalism and for setting an example of how to be an approachable department head and mentor.

I must also thank the Lhoist mining engineers and management for their boundless support throughout this project.

I acknowledge NIOSH for funding this project, and specifically I thank Dr. Brent Slaker and Dr. Michael Murphy for their feedback, recommendations, and for hosting and promoting research conferences to bring together this sector of the mining industry.

I would also like to thank Dr. David Hanson from NIOSH for working with me closely to advance GPR research. Dr. Hanson has been a valuable mentor, taking every opportunity to ask questions and sparing no time to seek out answers.

I would like to acknowledge Dr. Dean Goodman for developing the GPR-SLICE software as my research demanded, and for encouraging excellence throughout the process.

I must also thank my research group and the friends I have made at Virginia Tech. Juan Monsalve, Richard Bishop, Amin Abbasi, Dr. Marina Mullendore, Dr. Ali Haghighat, Manuel Barros Daza, Eleanor Pitcher, Eleftheria Agioutanti, Joe Tabor, Setareh Afrouz, Nestor Santa, Ava Menza, Dr. Kyle Louk, and many others have been constant sources of encouragement, laughter, and respite. They have inspired greatness in my work and have brought joy into my life.

Finally, I would like to thank my family. Mom, Dad, Sam, Rachelle, Noah, Leslie, Grace, Jake, and most recently, Zoey: always remember there is nothing worth sharing like the love that lets us share our name.

TABLE OF CONTENTS

LIST OF FIGURES

LIST OF TABLES

PREFACE

This thesis is comprised of three chapters, each detailing a specific case-study with its own unique use of ground penetrating radar (GPR) in an underground stone mine.

Chapter 1 describes the benefits and limitations of GPR as the geophysical method of choice for karst void detection and mapping in an underground mining scenario. In this chapter, a 2D GPR survey that was carried out by the research team in 2018 is described, as well as the processing methods in software. The conclusions of this chapter include proof of the concept of underground GPR surveys for long –range (~20 meter) karst void detection at the case study mine. The outputs of the case-study survey serve as direct influences for the case-study in Chapter 2.

Chapter 2 translates the conclusions of Chapter 1 into design parameters and survey inputs for a 3D GPR survey at the same location. The implications of karst void geometry on pillar strength estimations are discussed, with references to how pillar strength estimations in similar environments have developed through empirical research. The case-study includes novel GPR processing methods that had been carried out in the software (GPR-SLICE) for the first time ever, according to the software developer. Finally, recommendations for future work using similar designs as the case-study are included in hopes that the benefits of these surveys may begin to be used in the underground stone mining industry.

Chapter 3 involves the use of the Terravision GPR cart, which was donated for research use by the National Institute of Occupational Safety & Health (NIOSH). Using the cart, a case-study is performed in an underground multi-level mine to inspect the sill pillar between levels for anomalies, before the sill pillar is eventually blasted out and ultimately recovered. This work is the first of its kind to use the Terravision in an underground mine, and the results show both the successes and limitations that were observed.

Chapter 1: GROUND PENETRATING RADAR FOR KARST DETECTION IN UNDERGROUND STONE MINES

Jonathan Baggett, Virginia Tech, Blacksburg, VA

Amin Abbasi Baghbadorani, Virginia Tech, Blacksburg, VA

Juan Monsalve, Virginia Tech, Blacksburg, VA

Richard Bishop, Virginia Tech, Blacksburg, VA

Nino Ripepi, Virginia Tech, Blacksburg, VA

John Hole, Virginia Tech, Blacksburg, VA

Paper originally published as a preprint in the proceedings of the 2019 Society for Mining, Metallurgy, & Exploration Conference, February 24-27, 2019.

Abstract

This work focuses on the operational and safety issues associated with karst voids in large opening underground mines. Issues include water inrush, structural instability, and engineering uncertainty in these environments. Coupled with the fracturing prevalent in folded sedimentary rocks, karst voids are complex and challenging ground control risks.

Traditional methods of predicting karst void locations, such as probe drilling, are impeded by the inconsistent spatial distribution and variable sizes of the features. Ground penetrating radar (GPR) is a geophysical technique that transmits radio waves into a medium and subsequently detects reflected waves via a receiver. The travel time and energy of received signals are then processed and interpreted. The difference in material properties between limestone and open karst voids causes strong reflections.

GPR is frequently used as a geophysical surveying technique in several industries, however there is a lack of published research on underground mining GPR applications. The purpose of this work is to prove the viability of GPR in underground stone mines for karst void detection, and to discuss the importance of karst void detection ahead of mining.

1. Introduction

The Mine Safety and Health Administration (MSHA) currently lists 116 active underground stone mines in the United States, the vast majority of which extract limestone for crushed stone products. These limestone mines have the potential to encounter karst voids at some point in their operation, as most karstic regions of the United States develop in limestone rock masses (Kuniansky, Weary, & Kaufmann, 2016). Karst voids, the cavities formed by the dissolution of carbonate rock, have long plagued the mining and tunneling industries, as well as been a hindrance on the Earth's surface, producing sinkholes and ruining otherwise valuable land for construction and public use. The impact of karst voids on the Gavarres tunnel in Spain is well documented by Alija et al; constant instability conditions, material spills into the tunnel, and unexpected cavities seriously delayed the project deadlines and "were not foreseen in the design" (Alija, Torrijo, & Qunita-Ferreira, 2013). At the water

supply project in Sohngua River, China, Bin et al detail the presence of both water and sediment filled karst voids which are sources of disastrous conditions at this tunnel (Bin, et al., 2017). A hydrological tunnel in Lebanon encountered numerous massive karst voids in the tunneling path which required remediation via friction anchors, rockbolts, welded wire fabric, channel steel arch segments, invert steel beams, and shotcrete (Leech, Jaoude, & Ghanem, 2008). From a design standpoint, rock mass classification schemes, such as the RMR from Bieniawski and the Q-system from Barton, are not able to represent the true nature of a karstified carbonate rock mass, and therefore complex case-by-case analyses of underground conditions are necessary (Andriani & Parise, 2017).

Ground penetrating radar has been well understood and frequently employed in geophysical research studies since its first uses in glacier studies by Stern in 1930 (Slob, Sato, & Olhoeft, 2010). With applications ranging from rebar detection in concrete structures to buried grave identification in historical cemeteries, GPR's unique advantages have been widely identified and utilized (Slob, Sato, & Olhoeft, 2010). The first sophisticated GPR system was constructed by Geophysical Survey Systems, Inc. and its benefit was demonstrated by surveying ice-cored hills in Tuktoyaktuk, Canada (Annan & Davis, 1976). Today in 2018, a wealth of knowledge in the form of textbooks, scholarly articles, and case studies exist that have evolved the straightforward radar technology into a well-respected 3-dimensional imaging tool and quantitative estimator of medium properties (Slob, Sato, & Olhoeft, 2010).

Through electromagnetic wave propagation, GPR systems are capable of accomplishing the detection of dielectric boundaries within a solid medium, such as a rock mass or concrete structure. Conductive mediums highly attenuate the GPR wave energy, such as wet clays and soils, while dry, homogenous, resistive mediums are ideal for strong transmitted and received signals (Annan & Davis, 1976).Working in both ideal and problematic mediums, GPR has been demonstrated to map fractures in ornamental gneiss (Grasmueck, 1996), map soil stratigraphy and bedrock depth (Davis & Annan, 1989), and even to determine surface electrical properties on Mars and the moon (Simmons, 1972). The most common modern use of GPR is in concrete and asphalt imaging for construction and civil engineering uses, detecting the locations of rebar and metal structures as well as paving thickness and discontinuities (Hasan & Yazdani, 2016).

There are many successful examples of GPR being used in tunnels to predict conditions ahead of the working face and tunnel boring machine. Weidong et al demonstrate with a 100 MHz system the detection of loose rock due to blasting, broken up rock 18 meters behind the working face, and fissure water (Weidong, Fancheng, Renguo, Yonglei, & Zhengbo, 2012). Wang et al conducted a GPR survey on the walls of a tunnel to detect vertical shafts successfully (Wang, Zhang, Ren, Wu, & Peng, 2012). NIOSH has conducted research demonstrating GPR's capability to detect the extent of the spread of grout pumped into a tunnel roof, a common ground control technique and hazard remediation practice in tunneling and mining (Monaghan & Trevits, 2004). In his extensive doctoral dissertation, Oleg N. Kovin details his uses of GPR in potash mines to map stratigraphy, estimate the thickness of the overlying water-protective beds, characterize fractures, detect unstable roof rock, and evaluate the integrity of supporting pillars in the potash rock (Kovin, 2010). These studies assert the viability of GPR as a monitoring and investigative tool in underground excavations.

At this case study mine, management personnel indicated that it would be advantageous for their operation if they could use GPR at an active face for geologic forecast. Their blasting design would benefit if voids could be detected roughly 5-10 meters beyond the face. Part of this investigation examines the relationship between penetration depth of radar waves and resolution of data received.

2. Methodology

2.1 Case Study Mine

The case-study mine for GPR surveying is an underground multi-level room and pillar limestone mine. The ore body is synclinal, dipping at 30°; at present, the deepest level of the mine is approximately at the bottom of the syncline. The limestone orebody is roughly 30 meters thick. The current tunneling design allows for two 12-meter wide, 8-meter tall tunnels separated by 24-meter wide square pillars to safely extract as much of the seam as possible. As seen in Figure 1.1, the rock between the hanging wall tunnel of an upper level and the foot wall tunnel of the level below is eventually fully stoped-out. This mining method is appropriate for most of the upper levels of the mine, however adjustments to the number of tunnels and necessary pillar orientations are obvious in the lower levels where the dip of the orebody flattens and the syncline bottoms out.

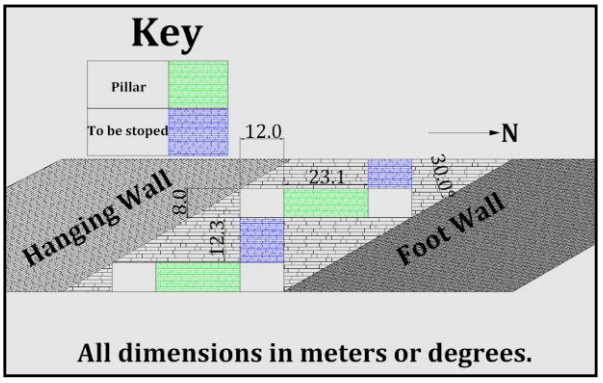

Figure 1.1 - Mine Model

Karst voids are found throughout the rock mass with spatial frequency that varies from level to level. These voids range in size from narrow and closed to extensive, wide aperture caves. They are typically planar and perpendicular to the mine tunneling direction; debris, consisting of residual clay and rock blocks, caves into the mining tunnel when production blasts breach the void. Figure 1.2 shows a laser-scan taken within a mine tunnel around a pillar and directly underneath of a protected karst void opening in the tunnel roof. The vertical extent of this void and the propensity of void-bound material to cave into the tunnel create a challenging ground-control risk, which in this case forced a deviation in the tunneling geometry, as is the reason for the triangular pillar.

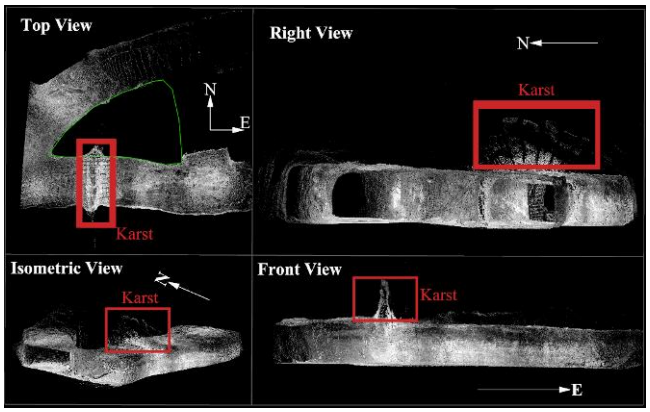

Figure 1.2 - Views of Case Study Pillar & Karst Void

Karst void formation occurs as slightly-acidic water comes into contact with carbonate rock; the conduits for water flow in this rock mass are the structural discontinuities present due to the folding of the sedimentary layers over geologic time; in the tunnel seen in Figure 1.2, the discontinuities have been mapped and characterized via LiDAR and geotechnical software programs in a previous work (Monsalve, Baggett, Bishop, & Ripepi, 2017). That study found four predominant joint sets in the tunnel, including one with a characteristic dip of 88° and a dip direction of 255°; the planar karst void in Figure 1.2 undoubtedly formed along a fracture represented by that joint set. Figure 1.3 is a picture taken on the hanging-wall tunnel side of the triangular pillar; steel straps, rock bolts, and plastic mesh were installed in the roof to keep unwanted material from falling into the tunnel. Figure 1.4 is a picture taken on the foot-wall tunnel side of the triangular pillar, where the only signs of the void are two closed discontinuities belonging to the previously mentioned joint set with excess residual clay coloring, characteristic of karst voids in this mine. Figures 1.3 and 1.4 suggest that these two closed discontinuities transition into an open void at some location within the pillar, eventually merging into the massive open void on the hanging-wall tunnel side of the pillar.

Figure 1.3 - Hanging-Wall Side of Triangular Pillar

Figure 1.4 - Foot-Wall Side of Triangular Pillar

The two closed planes can be seen and characterized from the same laser scan as seen in Figure 2; using Maptek's I-Site Studio 6.1 software, the dip and dip direction of these planes can be found, as seen in Figure 5. As suspected, the planes steeply dip at roughly 80°.

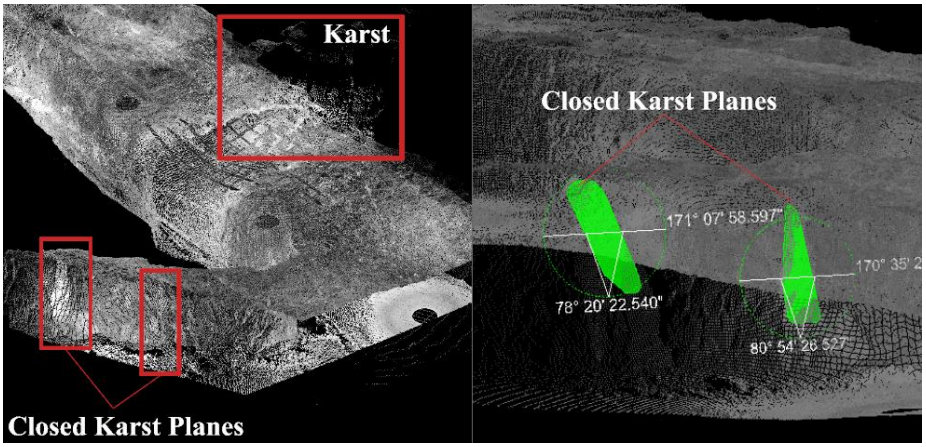

Figure 1.5 - Dip and Dip Direction of Karst Void Plane

The orientation, aperture, and extent of the karst void within the pillar cannot be analyzed visually, and cannot be accurately predicted due to the chaotic spatial variance of karst void sizes throughout the mine. These properties are the targets in the GPR surveys which constitute this study.

2.2 GPR Surveying Underground

A series of two-dimensional GPR surveys were conducted around the triangular pillar at different antenna frequencies to compare depth of penetration and resolution between surveys. The frequencies used were 200 MHz, 250 MHz, 500 MHz, and 1 GHz; all antennas are from Sensors & Software, and all are shielded with the exception of the 200 MHz pulseEKKO antenna. Lower frequency surveys offer deep penetration with low relative resolution, while higher frequency surveys offer high resolution at shallow depths. Shielded antennas have a conductive 'shield' behind the transmitter and receiver to prevent electromagnetic waves from traveling backwards and to direct energy solely into the desired medium; the use of shielded antennas in a mine tunnel is necessary for accurate data collection, as the rock wall / roof opposite the survey wall / floor is a strong, nearby reflector.

Traditionally, a GPR survey would traverse the ground surface in a straight line, and the shot locations of the survey would be ascertained from GPS systems or by dividing the survey line by the shot spacing of the GPR system. In these case-study surveys, the survey needed to traverse the pillar rib along a line projected onto the irregular pillar surface in an environment with no real-time positioning systems. For the 200 MHz and 250 MHz survey, this was accomplished with a simple surveying ribbon anchored to the rock face, as seen in Figure 1.6. The height of the survey was roughly one meter above the tunnel floor, however there was a berm with varying heights of material at the foot of the pillar.

Figure 1.6 – Low Frequency Survey Setup

The ribbon was marked every ten centimeters, which was the step size between signal pulses for both the 200 MHz and 250 MHz surveys. The survey traverse lines are seen in Figure 1.7.

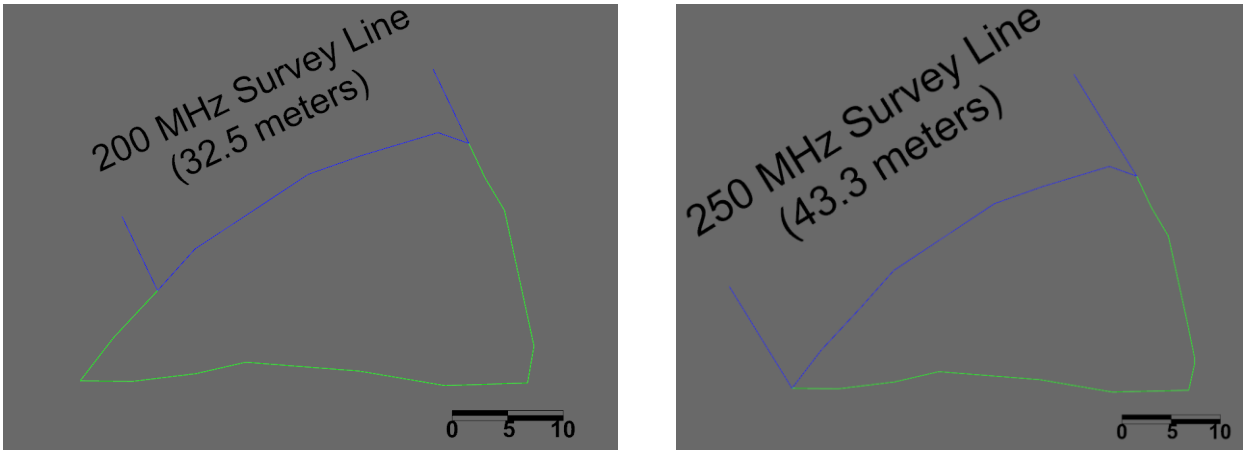

Figure 1.7 – 200 MHz & 250 MHz Traverse Lines

Antennas were mounted into a harness apparatus that the researchers fabricated out of PVC. One researcher positioned the two antennas perpendicular to the face along the survey ribbon while the second researcher would manually trigger each radar pulse and alert the first researcher when he could move on to the next mark on the survey ribbon. The survey parameters for 200 MHz and 250 MHz can be seen in Table 1.1, and the GPR harness can be seen in Figure 1.8.

Table 1.1 - 200 MHz & 250 MHz Survey Parameters

Freq. (MHz)	Survey Length (m)	Traces	Points per Trace	Antenna Spacing (m)	Stacks
200	32.5	324	1875	0.5	32
250	43.3	397	2750	0.25	64

Figure 1.8 – 200 MHz Survey in Progress

The design for the 500 MHz and 1 GHz surveys was not the same as the 200 MHz and the 250 MHz, as the higher-frequency antennas have smaller spacings along the survey line (five centimeters for 500 MHz, one centimeter for 1 GHz) which make manual-triggering and positioning difficult and prone to operator error. To avoid these inaccuracies, researchers opted for a wheel-trigger to accompany the high-frequency antennas during surveying which would automatically trigger the transmitting antenna based on an odometer. The irregularity of the pillar face was not an ideal track for the wheel-trigger, so 2.4-meter long wooden planks were fixed onto the pillar rib with small anchor bolts and zip-ties, so that the antennas and wheel-trigger would have a smooth, consistent surface to pass-over. The total length of the 500 MHz and 1 GHz surveys was considerably shorter than the 200 MHz and 250 MHz survey lengths because of the reduced penetration depth; the surveys were extended only as far as to encompass both of the closed karst void planes. Also, both the 500 MHz and 1 GHz surveys were divided into multiple 2.4-meter long lines, starting and ending completely on each wooden plank.

As planks were constantly being taken down and put up in the next surveying location, permanent record keeping of plank location and orientation with respect to the pillar rib was required to later ascertain the precise shot locations for the high-frequency surveys. To accomplish this goal, laser scans of the planks were conducted, stitched together, and finally referenced and automatically-registered in I-Site Studio 6.0 via reference points to the tunnel point cloud seen in Figure 1.5. The merged tunnel and plank point clouds can be seen in Figure 1.9.

Figure 1.9 - Planks Merged with Tunnel

After researchers previewed the 500 MHz data, the 1 GHz survey was designed with two additional plank locations following the final plank location of the 500 MHz survey; this was to try and better image an interesting reflection region seen near the end of the 500 MHz data. The survey traverse lines are seen in Figures 1.10 and 1.11. Corresponding survey parameters for the higher-frequency antennas are seen in Table 1.2.

Table 1.2 – 500 MHz & 1 GHz Survey Parameters

Freq. (MHz)	Survey Length (m)	Traces	Points per Trace	Antenna Spacing (m)	Stacks
500	19.2	398	3300	0.155	16
1000	24.0	2421	2200	0.075	16

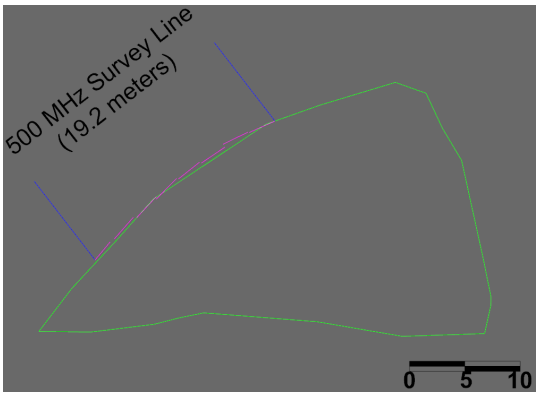

Figure 1.10 – 500 MHz Traverse Lines

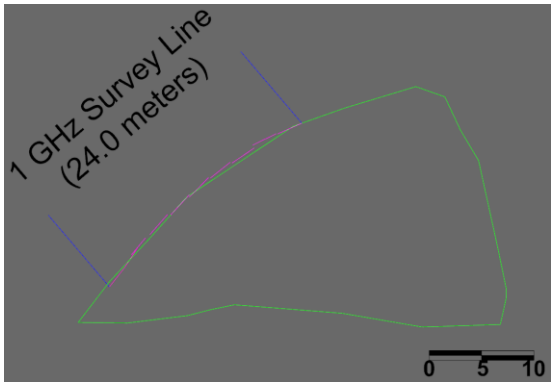

Figure 1.11 – 1 GHz Traverse Lines

3. Results and Discussion

Data processing was carried out using GPR-SLICE Ground Penetrating Imaging Software. Before any processing or interpretation could occur, point locations for each GPR shot had to be recorded and input into GPR-SLICE along with the raw reflection data. Shot locations were determined by dividing the traverse lines seen in Figures 1.7, 1.10, and 1.11 by the total number of traces, then exporting the nodes of the divided traverse lines as points in an XYZ format. Pitch and yaw of the antennas were intentionally avoided as much as possible by aligning the antenna faces perpendicular to the survey line, and therefore were not incorporated into the input location files. Raw radargrams were produced, as seen in Figures 1.12 through 1.14.

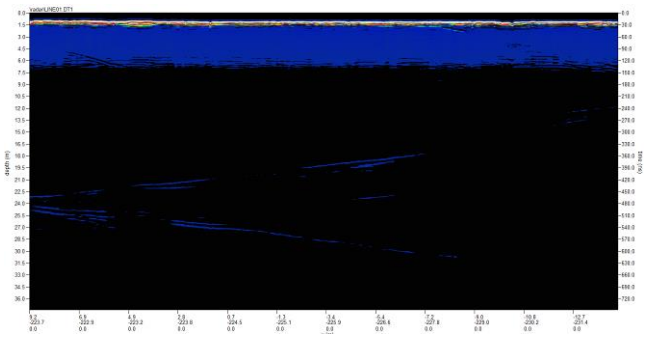

Figure 1.12 - 200 MHz Raw Radargram

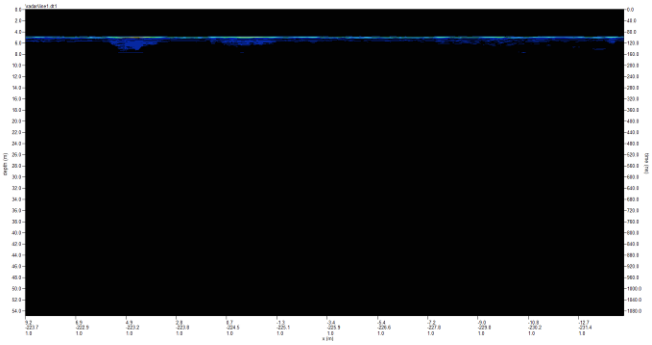

Figure 1.13 – 250 MHz Raw Radargram

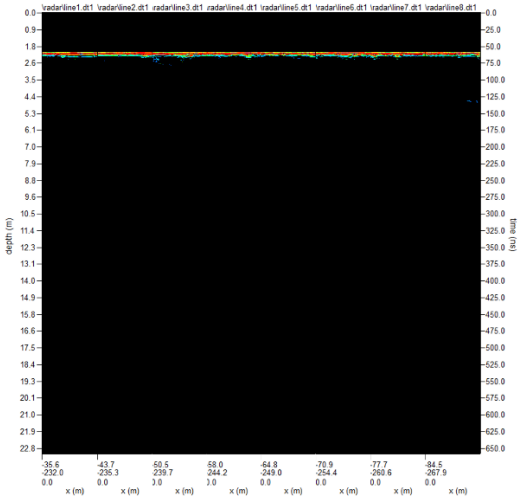

Figure 1.14 - 500 MHz Raw Radargram

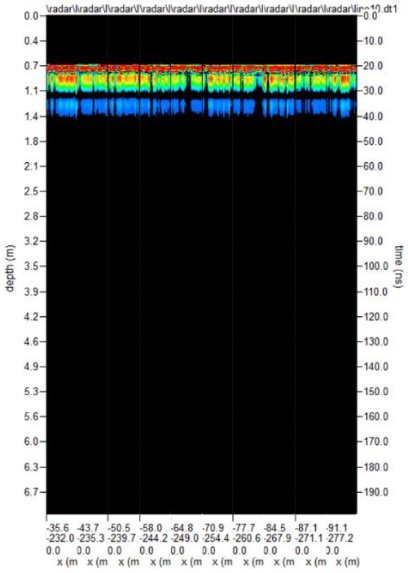

Figure 1.15 –1 GHz Raw Radargrams

The radargrams in Figures 1.14 and 1.15 are the merged individual radargrams for each of the high-frequency wooden plank survey lines. The y-axis on all radargrams is time/distance (time is converted to distance with wave velocity in limestone). Speed of the radar wave in a medium is indirectly proportional to the square root of the *dielectric constant* of the medium via the equation:

$$\boldsymbol{velocity} = \frac{\boldsymbol{speed\ of\ light}}{\sqrt{\boldsymbol{dielectric\ constant}}}$$

The dielectric constant is the ratio of the permittivity of a material to the permittivity of free space; limestone has a dielectric constant range of about 4-8 (Parkhomenko, 1967). Rather than conduct time-consuming permittivity tests on representative core samples, a simple common-transmitter survey on the in-situ rock gives a plot of the direct-wave arrival time versus distance. The design of a common-transmitter survey at the triangular pillar is seen in Figure 1.16.

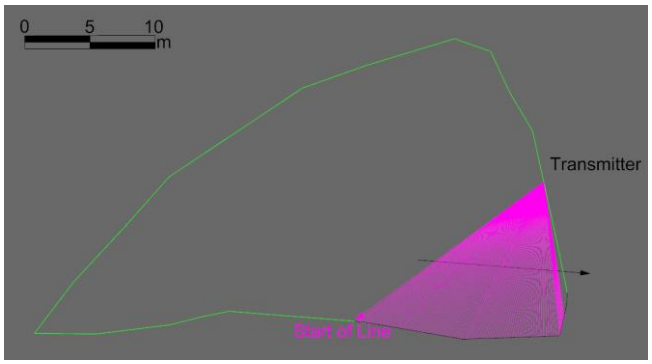

Figure 1.16 - Common Transmitter Survey

The transmitter remained fixed at the indicated location while the receiving antenna was moved from the 'start of line' point towards the corner of the pillar. The first arrival wave at the receiving antenna traveled directly from the transmitter in a straight line, and the distance from the transmitter to every receiver position is known, therefore the velocity of the wave in the pillar can be easily determined. No processing is required for this interpretation, so the radargram displayed by the GPR control console is shown in Figure 1.17 with the direct wave indicated.

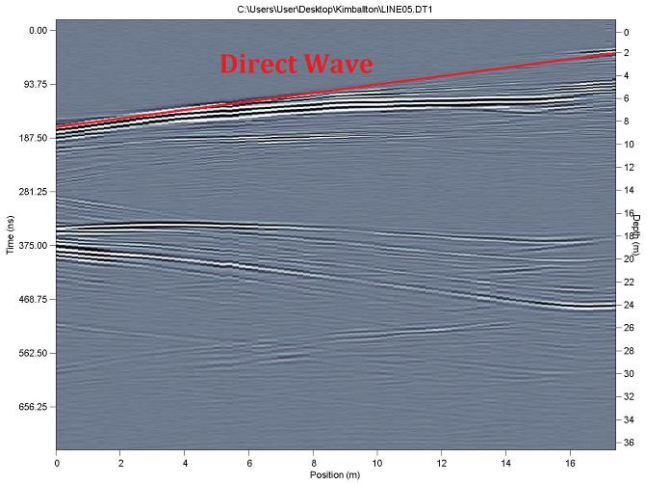

Figure 1.17 - Common Transmitter Survey Radargram

The velocity of the radar waves in the case-study pillar was determined to be roughly 0.10 m/ns, which implies a dielectric constant of 9, higher than expected for limestone. The y-axis of the reflection radargrams is converted to distance with the value of 0.10 m/ns.

As can be seen in Figures 1.12 through 1.15, the raw radargrams showed no discernible reflection horizons and for the most part showed nothing; several processing steps were required to correct the time/depth of the data, filter out unwanted frequency responses, apply gain to the signal which attenuates with depth, and filter out other unwanted effects that arise during the surveys. The processing flow applied to these surveys is:

1. Time-zero Correction
2. Background Filters
3. Bandpass Filters
4. Regain (as necessary)

The raw radargrams show a gap from time = 0 down towards the consistent horizontal reflection boundary; this boundary is where the radar wave encounters the pillar surface. Within this time range, the radar wave is actually traveling through air at the speed of light, therefore the plotted distance is inaccurate by a factor of 3 (actually travelling at 0.30 m/ns, plotted as 0.10 m/ns). Additionally, there is a built-in time delay before the receiving antenna begins recording reflections, which produces an exaggerated gap in the radargram. Furthermore, the desired reflection data lies within the pillar, so the radargrams should be corrected so that time = 0 occurs at the pillar surface reflection boundary. The time-zero corrected radargrams look nearly identical to the raw radargrams, only with all data shifted upwards.

Next, a background filter is applied to each radargram to remove horizontal banding which commonly appears in GPR data as noise from sources such as cellphones or communication networks (Wiseman & El-Baz, 2007). The effect of the background filter is largely unnoticeable until gain has been applied. Following the background filter, a bandpass filter is applied to filter out the reflected signal responses with frequencies outside of the operating band of each antenna. The reported frequency for a GPR antenna is actually a central frequency in a bandwidth sent out by the system; the frequency ranges for the four antenna systems used in this case study are seen in Table 1.3.

Table 1.3 - Antenna Bandwidths

Central Frequency (MHz)	Low-End Frequency (MHz)	High-End Frequency (MHz)
200	100	300
250	125	375
500	250	750
1000	500	1500

Processing gain is applied to the radargrams during the bandpass filtering process. The gain amplifies signals which have otherwise lost energy due to attenuation into the rock mass, and spherical spreading. Constant gain can be applied to the entire depth of the radargram, however it is more appropriate to apply more gain to the signals which have attenuated more (deeper signals). In GPR-SLICE, a linear, exponential, or custom gain curve can be constructed depending on the expected target depth and attenuation behavior of the radar waves. The time-zero corrected, background filtered, bandpass filtered, and gain applied radargrams can be seen in Figures 1.18-1.21.

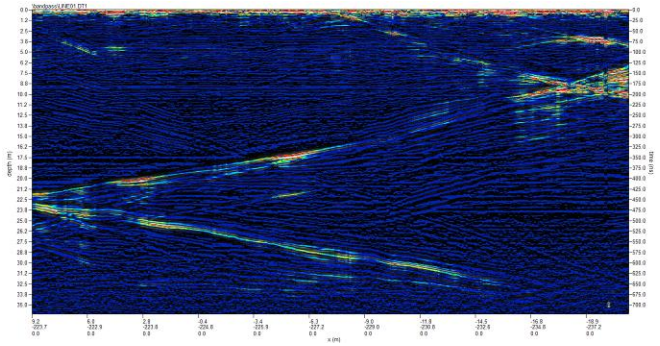

Figure 1.18 - 200 MHz Time-Zeroed, Background Filtered, Bandpass Filtered, and Gained

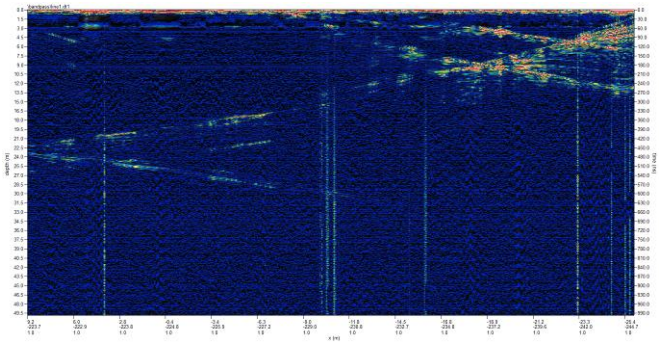

Figure 1.19 - 250 MHz Time-Zeroed, Background Filtered, Bandpass Filtered, and Gained

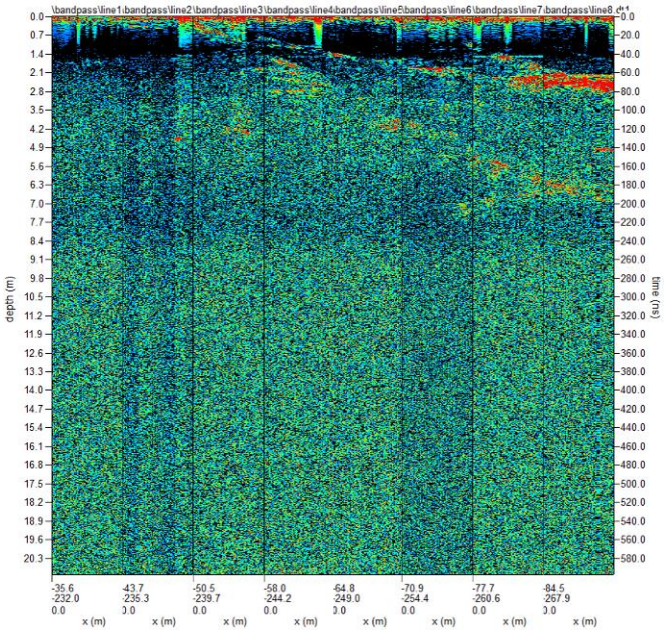

Figure 1.20 - 500 MHz Time-Zeroed, Background Filtered, Bandpass Filtered, and Gained

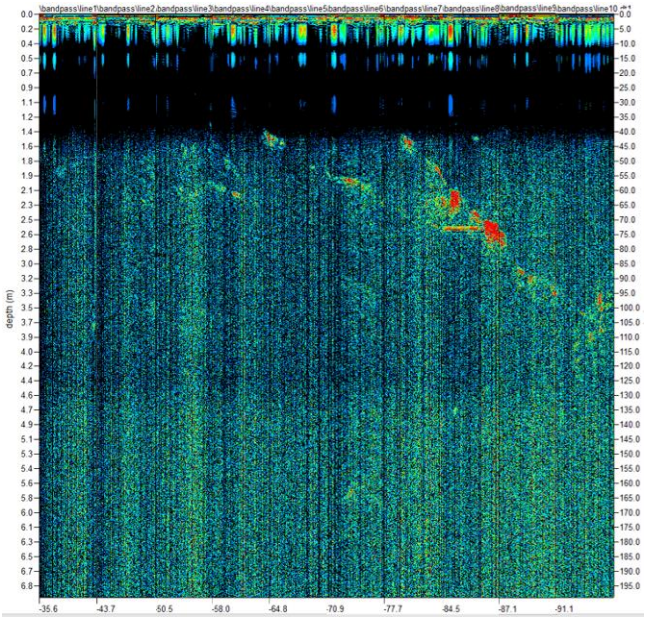

Figure 1.21 - 1 GHz Time-Zeroed, Background Filtered, Bandpass Filtered, and Gained

Once the radar data had been fully processed, reflection boundaries became clearly visible in each profile. Across all four frequencies, a dipping reflector towards the end of the radargram was visible; to interpret this consistency and to compare these surveys, they were plotted in their true spatial positions in reference to the pillar geometry. These plots are seen in Figures 1.22-1.25.

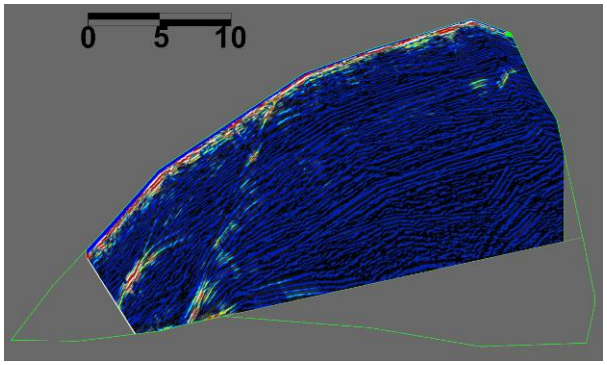

Figure 1.22 - 200 MHz in Pillar

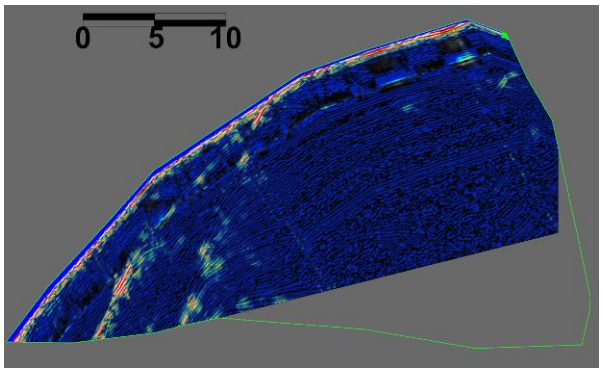

Figure 1.23 - 250 MHz in Pillar

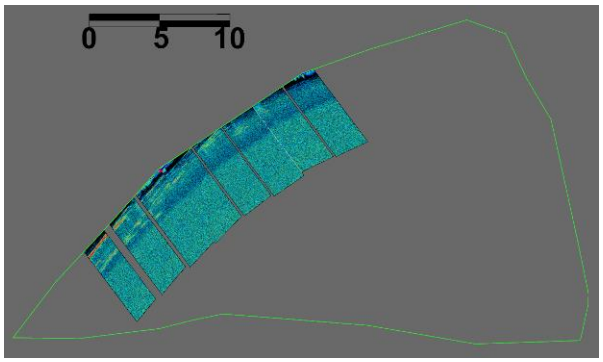

Figure 1.24 - 500 MHz in Pillar

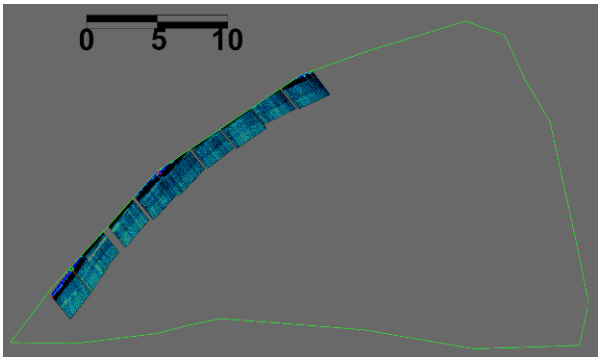

Figure 1.25 - 1 GHz in Pillar

The previous figures depict how penetration depth reduces as frequency increases; while the 200 MHz and 250 MHz surveys received strong reflection data throughout the pillar (around 11 meters depth for good signal), the 500 MHz survey became oversaturated with noise (bad signal) beyond 2.2 meters, and the 1 GHz survey encountered the same issue around 1.7 meters depth into the pillar. Due to this limitation, neither the 500 MHz nor the 1 GHz surveys were able to detect a consistent linear reflection representative of the karst void planes. Fortunately, both the 200 MHz and 250 MHz surveys show strong reflection boundaries off of two linear features within the pillar. The relevance of these boundaries becomes more obvious when the spatially plotted radargram is plotted with the pillar laser scan in the same view; this depiction is seen in Figure 1.26.

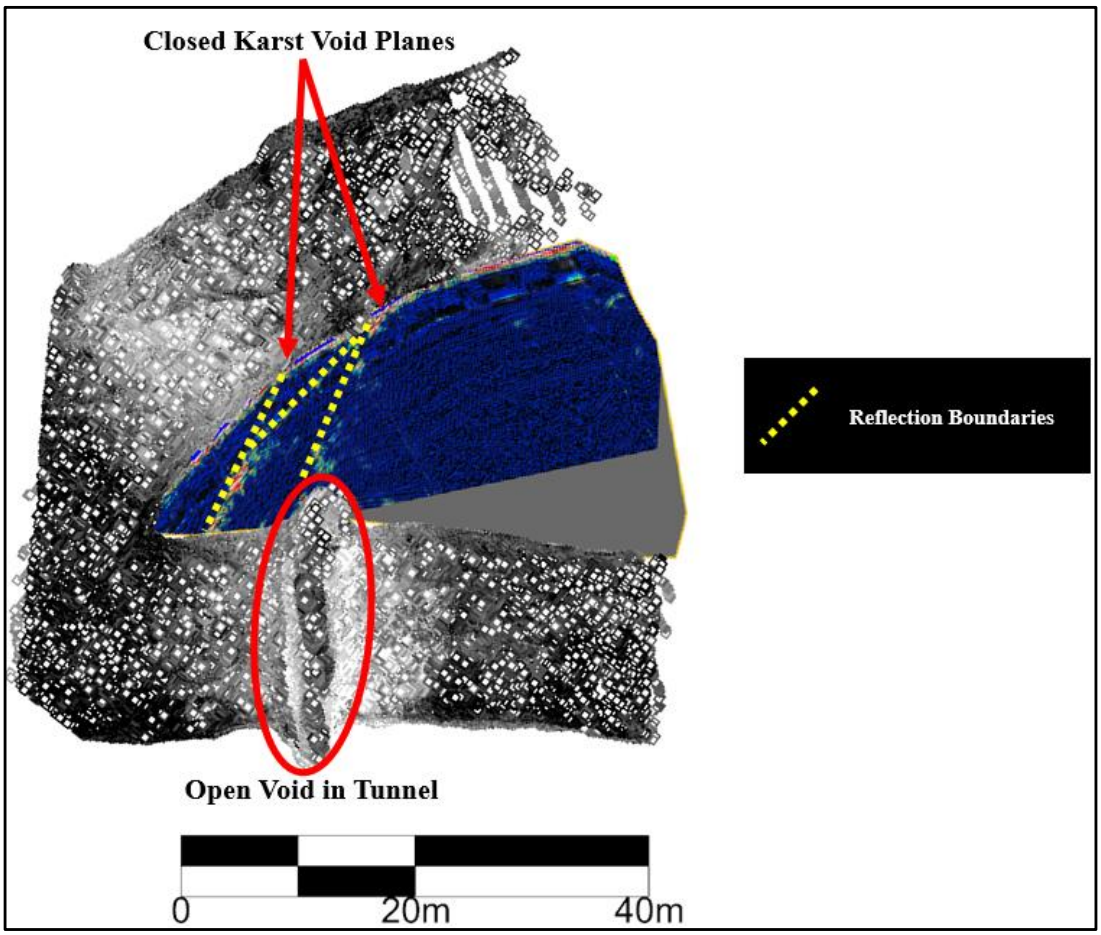

Figure 1.26 - Radargram Spatially In Reference to Pillar Point Cloud (Top View)

The planes suspected to connect to the open karst void clearly propagate through the pillar in Figure 1.26. Additionally, the reflection boundaries widen at depth and multiple clustered hyperbolae are seen before the boundaries terminate into the pillar wall. Somewhere in this clustering, the closed planes transition into open fractures and eventually into the open void. Unfortunately, the high-resolution survey quality needed to ascertain these transition locations was not attainable due to the limited depth of penetration for the 500 MHz and 1 GHz. Additional reflection boundaries are visible in the 200 MHz and 250 MHz surveys, one which appears to be a plane connecting the two closed karst void planes.

4. Conclusions

Karst voids may present ground control risks and hazards associated with water and caving material. The chaotic spatial randomness of karst void formation is a challenge for detecting, mapping, and predicting the size of voids. In this work, ground penetrating radar has been shown to detect karst features within a limestone pillar at depth, and the processed data offers inferences into the locations where these karst features expand into a large open void. The two-dimensional reflection survey has limitations in describing how the karst features are oriented at different heights within the pillar, therefore multiple surveys are needed to properly describe the karst void in 3D. Sophisticated

analyses, such as gridded 3D surveys on the pillar face, may offer inference into the volume of void space within the pillar.

Using the lower frequency antennas (200 MHz and 250 MHz) the karst voids were detected as far as about 11 meters from the pillar face. This depth of penetration satisfies the case study mine management's need for geologic forecast at an active face of around 5-10 meters. While some resolution in the reflected radar waves is not imaged with lower frequency surveys, the strong dielectric boundary between the limestone pillar and the void space was clearly visible in the 200 MHz and 250 MHz data at depth. Drilling into the pillar at the measured reflection locations could be a useful confirmation method.

5. References

1. Alija, S., Torrijo, F. J., & Qunita-Ferreira, M. (2013). Geological engineering problems associated with tunnel construction in karst rock masses: The case of Gaverres tunnel (Spain). *Engineering Geology*, 103-111.

2. Andriani, G. F., & Parise, M. (2017). Applying rock mass classifications to carbonate rocks for engineering purposes with a new approach using the rock engineering system. *Journal of Rock Mechanics and Geotechnical Engineering*, 364-369.

3. Annan, A., & Davis, J. L. (1976). Impulse radar sounding in permafrost. *Radio Science*, 383-394.

4. Bin, L., Zhengyu, L., Shucai, L., Lichao, N., Maoxin, S., Huaifeng, S., . . . Yonghao, P. (2017). Comprehensive surface geophysical investigation of karst caves ahead of the tunnel face: A case study in the Xiaoheyan section of the water supply project from Songhua River, Jilin, China. *Journal of Applied Geophysics*, 37-49.

5. Davis, J., & Annan, A. P. (1989). Ground-Penetrating Radar For High-Resolution Mapping of Soil and Rock Stratigraphy. *Geophysical Prospecting*, 531-551.

6. Grasmueck, M. (1996). 3-D ground-penetrating radar applied to fracture imaging in gneiss. *Geophysics*, 1050-1064.

7. Hasan, M. I., & Yazdani, N. (2016). An Experimental Study for Quantitative Estimation of Rebar. *Journal of Engineering*, 8.

8. Kovin, O. N. (2010). *Ground penetrating radar investigations in Upper Kama potash mines.* Missouri S&T.

9. Kuniansky, E. L., Weary, D. J., & Kaufmann, J. E. (2016). The current status of mapping karst areas and availability of public sinkhole-risk resources in karst terrains of the United States. *Hydrogeology*, 613-624.

10. Leech, W. D., Jaoude, I. B., & Ghanem, N. (2008). *Madiq Tunnel, Lebanon: TBM Tunneling vs. Karst Geology.* Beirut.

11. Monaghan, W. D., & Trevits, M. A. (2004). *Application of Ground Penetrating Radar to Evaluate the Extent of Polyurethane Grout Infiltration for Mine Roof Control.* Pittsburgh: NIOSH.

12. Monsalve, J. J., Baggett, J., Bishop, R., & Ripepi, N. (2017). Application of Laser Scanning for Rock Mass Characterization and Discrete Fracture Network Generation in an Underground Limestone Mine. *37th International Conference on Ground Control in Mining*, (pp. 183-192). Morgantown, WV.

13. Parkhomenko, E. I. (1967). *Eletrical Properties of Rocks.* Moscow, USSR: Institute of Physics of the Earth.

14. Simmons, G. (1972). The surface electrical properties experiment. *Lunar Geophysics*, 258-271.

15. Slob, E., Sato, M., & Olhoeft, G. (2010). Surface and borehole ground-penetrating-radar developments. *Geophysics*, 103-120.

16. Wang, Y., Zhang, Z., Ren, Q., Wu, Y., & Peng, Z. (2012). Application of LTD-2100 Ground Penetrating Radar to Advanced Forecast in Diversion Tunnel of Jinping Hydroelectric Power Station. *14th International Conference on Ground Penetrating Radar* (pp. 57-61). Shanghai: IEEE.

17. Weidong, P., Fancheng, M., Renguo, G., Yonglei, L., & Zhengbo, H. (2012). Relationship Between Operation Technology of Ground Penetrating Radar and Precision of Advanced Forecast. *International Conference on Computer Science and Electronics Engineering* (pp. 640-644). IEEE.

18. Wiseman, J., & El-Baz, F. (2007). *Remote Sensing in Archaeology*. Boston, MA: Springer Science + Business Media, LLC.

Chapter 2: A 3D GROUND PENETRATING RADAR SURVEY OF KARST VOIDS IN AN UNDERGROUND LIMESTONE MINE PILLAR

Jonathan Baggett, Virginia Tech, Blacksburg, VA

Amin Abbasi Baghbadorani, Virginia Tech, Blacksburg, VA

Nino Ripepi, Virginia Tech, Blacksburg, VA

John Hole, Virginia Tech, Blacksburg, VA

Abstract

This work summarizes a series of 3D ground penetrating radar (GPR) surveys for karst void mapping within a mine pillar in a large opening underground limestone mine. In this case study mine, karst features are hazardous ground control risks that interact with geologic discontinuities, creating free blocks within the rock mass. As tunnels are advanced via blasting, unknown karst voids may be exposed and pose risks to mining personnel. The voids also form a hydrogeological network of water reservoirs with spatial locations throughout the rock mass that are difficult to predict with traditional methods such as drilling.

Karst void detection at a fixed height in this pillar was carried out in a previous work (Baggett J. G., et al., 2019) as a proof of concept for future works to utilize similar GPR methodologies; this work expands on that concept and further investigates the surface shape of the same karst void via a dense grid of 3D GPR data. As has been established in that previous work, the homogenous limestone at the case study mine is an ideal medium for GPR, with negligible attenuation characteristics, little conductivity, and significant contrast in material properties between open karst voids and solid limestone rock.

While GPR has been utilized throughout several industries for anomaly detection, mapping, and validating other geophysical datasets, this technique has not seen the same proliferation within the mining industry. Regarding published literature, there is a lack of works that detail the applicability of GPR in underground mining scenarios. The aim of this work is to expand on previous methodologies establishing GPR as a useful tool in underground mining applications, and to discuss the benefits and limitations of high-density 3D data in such scenarios.

1. Introduction

The underground stone mining industry in the United States provides crucial resources for the construction, agricultural, and environmental industries (Bliss, Hayes, & Orris, 2008). The sedimentary carbonate rock masses in which underground stone mines are excavated are prone to geologic folding and faulting, resulting in discontinuous structural conditions that may lead to roof falls during tunneling (Esterhuizen G. S., Dolinar, Ellenberger, Prosser, & Iannacchione, 2012). These discontinuities also may serve as hydrogeological conduits and consequently channels for karstification, the dissolution of carbonate rock (Parise, Gabrovsek, Kaufmann, & Ravbar, Recent advances in karst research: from theory to fieldwork and applications, 2018). The interactions between karst voids and geologic discontinuities create complex and hazardous conditions for underground excavations, and traditional rock mass characterization schemes may not adequately incorporate these conditions that are specific to carbonate rock masses; in recent years, attention has been focused on amending these classification schemes (i.e. RMR, Q-system) to better represent the in-situ conditions of complex carbonate environments (Andriani & Parise, 2017) (Waltham & Fookes, 2003).

For a room-and-pillar underground stone mine, karst voids may hinder engineered tunnel design, pillar layout, and excavation sequences. The ultimate stability of a mine section depends primarily on the strength of its pillars; empirical formulas for stone pillar strength based solely on the pillar width (w), height (h), and uniaxial compressive strength (UCS) have been suggested, such as the following (Roberts, Tolfree, & McIntyre, 2007):

$$S = 0.65 \times UCS \times \frac{w^{0.30}}{h^{0.59}}$$

To take into account the presence of angular discontinuities that intersect pillars, NIOSH simulated discontinuities at several different dip angles that cut through a pillar using two-dimensional discrete element method numerical analysis (UDEC) and analyzed the implications for pillar stability (Esterhuizen, Dolinar, & Ellenberger, 2011). It was observed that in scenarios where a large discontinuity dipping less than $70°$ intersected a mine pillar, the empirical formula above overestimated the pillar strength. An amendment to the formula was suggested, incorporating a discontinuity correlation factor called the "large discontinuity factor" (LDF):

$$S = 0.65 \times LDF \times UCS \times \frac{w^{0.30}}{h^{0.59}}$$

Furthermore, supplementary adjustments to these formulas have been recommended in scenarios involving rectangular pillars (Wagner, 1992). Limitations to these formulas have been discussed for scenarios involving weak bedding planes and moisture (Esterhuizen G. S., AN EVALUATION OF THE STRENGTH OF SLENDER PILLARS, 2007). Additionally, in the case study mine for these GPR surveys, individual pillar shapes and tunnel layouts were observed to be irregular and often dependent on the presence of voids, and representative widths could be difficult to ascertain. A truly representative estimation of pillar strengths in such an environment requires a better understanding of the structural discontinuities within the pillar, the geomechanical characteristics of the rock and the discontinuities, the true geometry of the pillar, and karst voids that may be hidden from view.

In recent years, terrestrial LiDAR has been utilized for comprehensive geotechnical analyses in underground mining scenarios, assisting engineers in rock mass characterization and allowing for comprehensive summaries of discontinuity characteristics, such as location, orientation, spacing, persistence, and variability (Kemeny & Donovan, 2005) (Mah, 2012) (Monsalve, Baggett, Bishop, & Ripepi, 2017). Furthermore, this information may be summarized as discrete fracture networks (DFN's), which can reproduce statistically representative discontinuities for a number of purposes, including numerical simulations of underground mining scenarios (Lorig, Darcel, Damjanac, Pierce, & Billaux, 2015). Karst features also have been studied using LiDAR to accurately detail their surfaces as a means of predicting their initial formation and overall development (Guo, et al., 2018).

In scenarios where karst voids are visible on mine pillar surfaces, a sophisticated geometrical model incorporating joint sets and karst feature geometry can be obtained via technologies like LiDAR and DFN generation software, but if the void is 'hidden' within the rock, the true geometry of the pillar will not be accurately represented with these methods alone. Geophysical methods have seen great proliferation for anomaly detection within mediums, and GPR specifically has been proven useful especially for karst void detection and mapping (Ballard, Cuenod, & Jenni, 1982). While GPR may be limited in applicability due to the dielectric material properties in the medium through which the electromagnetic waves propagate, limestone in general is resistive and an ideal material to survey with GPR (Annan A. P., 2002). A resistive medium results in low attenuation and relatively little energy absorption into the medium, resulting in greater depths of penetration and strong reflected signal amplitudes. Typical GPR systems for geologic anomaly detection have central frequencies ranging from 125 MHz – 1 GHz (GPR Systems & Surveying Equipment, 2019).

2. Methodology

2.1 Survey Area

All GPR surveys were carried out in a large-opening underground stone mine which utilizes the room-and-pillar tunnel design method on multiple mine levels. The case study mine has been described in previous works (Monsalve, Baggett, Bishop, & Ripepi, 2017) (Baggett J. G., et al., 2019), and the surveys described in this work were performed on the rib of one pillar at the mine. A karst void can be seen visibly intersecting through the pillar, and a 2D GPR survey was carried out to detect the karst void's location within the pillar at a height of 1 meter from the tunnel floor. Figure 2.1 shows a plan view of the pillar as well as an estimation of the void's position based off of the previous study (Baggett J. G., et al., 2019). The pillar is roughly 8.5 meters tall.

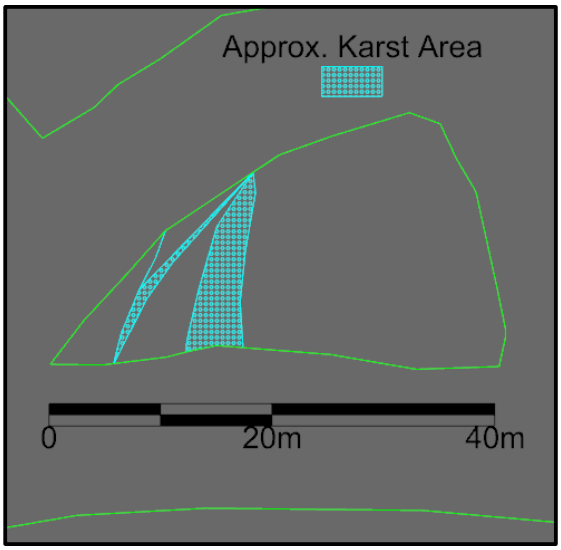

Figure 2.1 - Plan View of Surveyed Pillar

2.2 Survey Design

3D surveying requires a set of gridded lines with shot locations that can be accurately mapped and referenced, but the pillar rib had a highly irregular surface that could not be smoothly surveyed for either horizontal or vertical directions. This limitation implied that a separate surface overlaid onto the rib was needed to have survey lines that could be accurately mapped. The authors decided to use a 3-meter square tarp marked with survey lines and shot locations, to hang the tarp from the top corner grommets onto anchor bolts drilled into the rib, and to map the survey lines and shot locations in a 3D space by laser scanning each tarp position; a total of 8 tarp positions were surveyed. The anchor bolts were later surveyed and used as geo-referencing objects. A picture of the tarp hung up on the rib is seen in Figure 2.2.

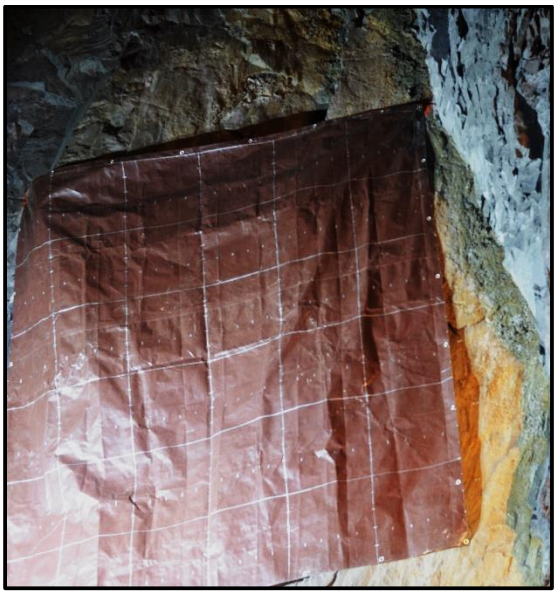

Figure 2.2 - GPR Surveying Tarp

Line spacing was 0.5 meters in both horizontal and vertical directions. A 250 MHz antenna was selected based off of the previous study, as this frequency showed a penetration depth of greater than 20 meters and resolution was favorable; for 250 MHz, the recommended step size between shots for the 250 MHz Noggin GPR system from Sensors & Software used for these surveys was 0.1 m (Software, 2019). While seven vertical survey lines could be accurately surveyed on the tarp, only six horizontal lines could fit, as the grommets at the top edge of the tarp prevented the authors from pre-marking the necessary shot positions.

Furthermore, the entire length of each horizontal could be surveyed for all 31 shot positions, while the vertical lines could only be surveyed up to the first 28 shot positions due to the same issue. For a set of 6 horizontal and 7 vertical lines with 31 and 28 shots each respectively, 382 shots were required to full survey each tarp position. Researchers used a manlift to access the tarp, as seen in Figure 2.3. The position of all 8 tarps with respect to the anticipated karst void location can be seen in Figure 2.4.

Figure 2.3 – Manlift

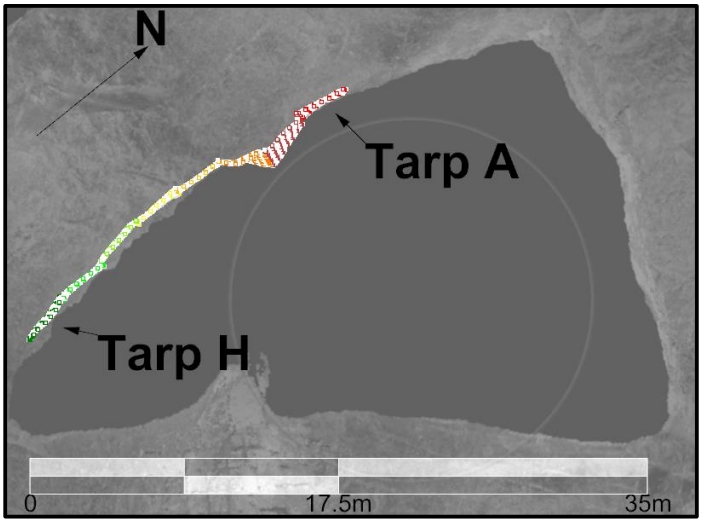

Figure 2.4 - All Tarps with Respect to Pillar

To properly map shot locations, attempts were made with both single-camera photogrammetry and terrestrial laser scanning to digitally record the tarp position when on the pillar. Both technologies are well established and demonstrated methods for 3D surface mapping, and for this study photogrammetry point clouds were constructed in Agisoft Photoscan, while laser scanned point clouds were imported into I-Site Studio 6.1 from Maptek. Figure 2.5 shows a tarp surface reconstructed via photogrammetry, and Figure 2.6 shows the same tarp as seen from a laser scan.

Figure 2.5 - Tarp Surface via Photogrammetry

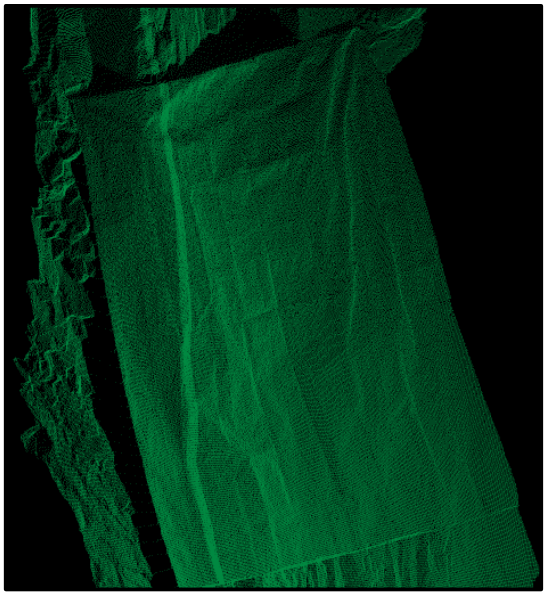

Figure 2.6 - Tarp Surface via Laser Scanning

The laser scanner did not collect color information for each point in the resultant point cloud, however the photogrammetrically constructed point cloud for the tarp retained the color and light information seen in the camera images; this gave the photogrammetric point cloud a considerable advantage, as shot location markers must be

identified by hand. The photogrammetric point cloud unfortunately had many errors due to the number of photos taken and the lighting underground; this resulted in an inaccurate representation of the tarp surface, making the laser-scanned point cloud better for picking shot markers. When the tarp was illuminated with handheld LED lights underground, the laser scanner was able to capture reflectivity along with point positions; in Figure 2.7, both the horizontal and vertical pre-marked survey lines are clearly seen in the laser-scanned point cloud. The hand-picked surveying points are also seen in Figure 2.7 in the image on the right.

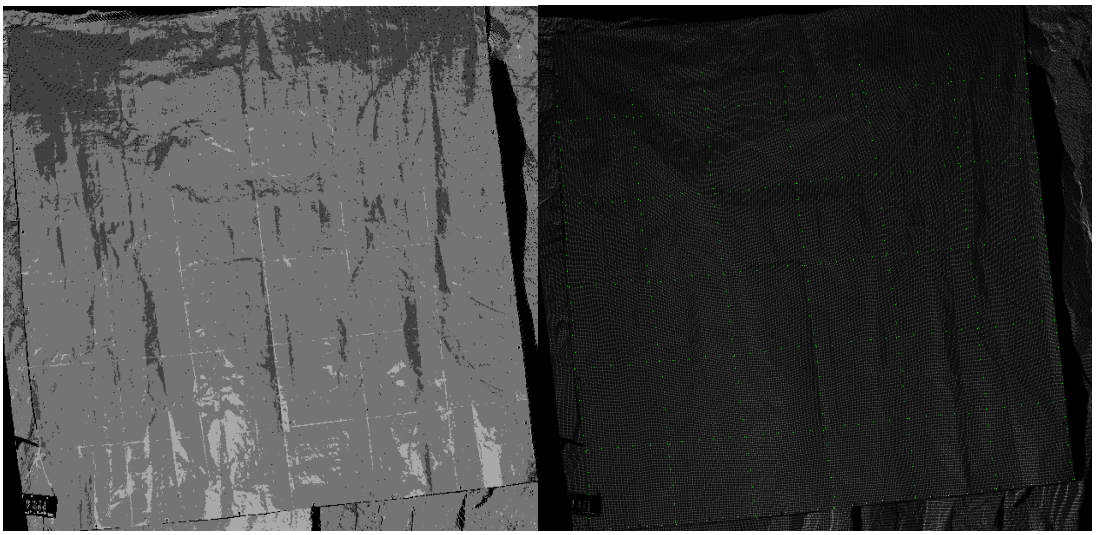

Figure 2.7 - Reflectivity in Laser Scan, Hand Picked Points

2.3 Surveying

3D surveying was conducted on May 21, 2018 through May 25, 2018. Antenna parameters used include 2750 points per trace, a time window of 1100 nanoseconds, and 64 stacks for each trace. Shots were manually triggered at 10 centimeter spacings, and all tarp positions were surveyed by two researchers using a man-lift. The Noggin 250 MHz system used for all surveying was shielded, implying that all the radar energy was directed, as intended, into the pillar. A laser scan was taken of each tarp position before the tarp was surveyed. Tarp positions were named A through H, corresponding to the beginning and ending position. Horizontal lines were named 1 through 6, from bottom to top, and vertical lines were named 1 through 7, from left to right. For example, the third horizontal line on tarp G and the fifth vertical line on tarp B would be named GH3 and BV5, respectively. This effort was a collaboration between the Mining Engineering and Geosciences departments at Virginia Tech. A picture of a survey in progress is seen in Figure 2.8.

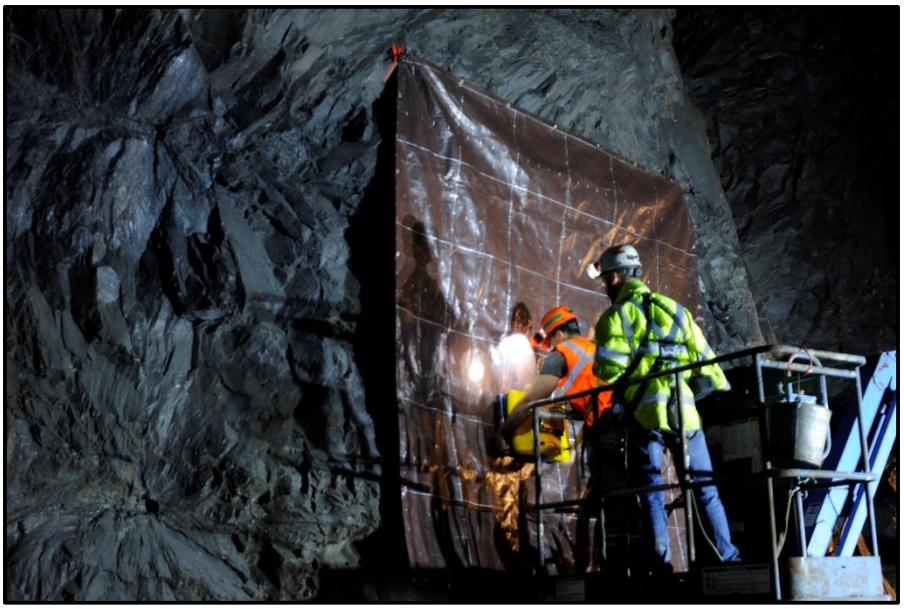

Figure 2.8 - 3D Surveying in Progress

3. Results and Discussion

3.1 Processing Flow

Raw data was organized by tarp position, and map files were generated from the manually-picked, laser-scanned shot locations. Pitch and yaw of the antennas were considered negligible. GPR-SLICE Ground Penetrating Imaging Software was used for all data processing, radargram imaging, interpolation, and isosurface generation. Data processing included (1) time-zero correction, (2) background filtering, (3) bandpass filtering, (4) gain, and (5) Hilbert transform. As the antenna surface is not directly couple to the mine pillar surface, there is some period of time during which the radar wave travels through air, and this time is canceled out via the time-zero correction. The time-zero corrections also corrects for the system time delay before the receiving antenna begins recording reflections. If there is a consistent source of noise in the data, such as external frequencies from communication signals, and the effects of this noise is seen throughout all traces in a survey line, this constant noise can be removed with a background filter. If there are isolated sources of noise in the data at frequencies outside of the antenna's bandwidth, these noise signals can be removed with a bandpass filter. As the radar waves travel through the rock mass, energy attenuates throughout the medium and the received signals are much weaker than the incident signals due to spherical spreading, so gain is applied to 'boost' the signal amplitude from deep reflections. The sinusoidal response signals received by the antenna may have both positive and negative frequency components, so to consider only the amplitude of these components and disregard the sign, the Hilbert transform is applied. A visual example of processing is seen in Figure 2.9.

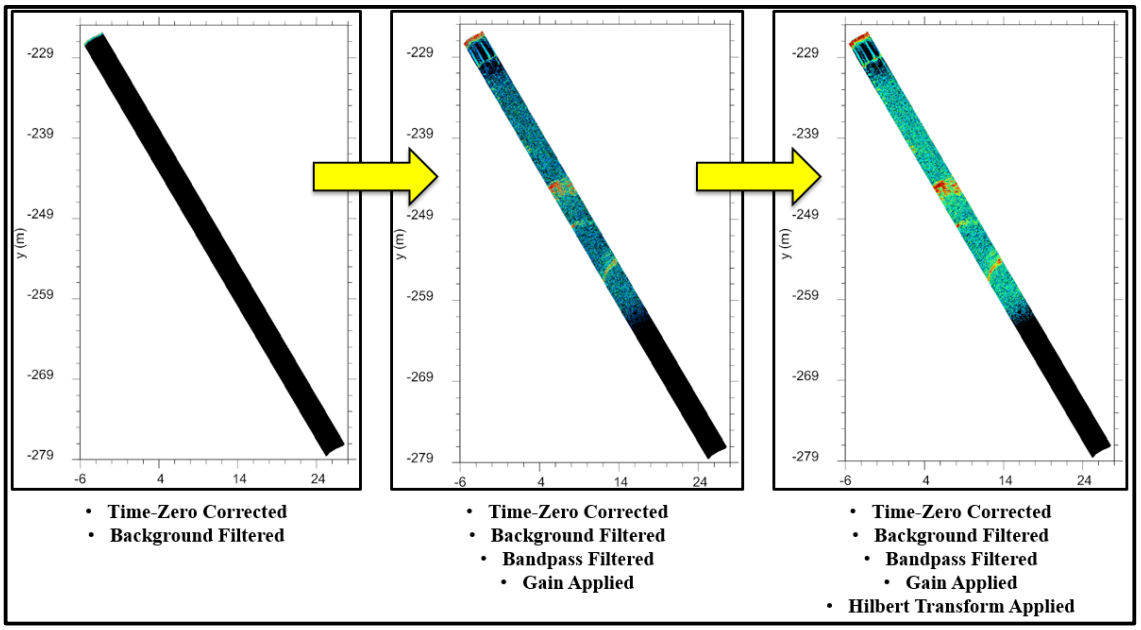

Figure 2.9 - Processing Flow Visual

As each tarp grid was processed individually, it was important to determine the plotting direction and orientation of radargrams. In a typical surface scenario, a GPR survey is conducted on a mostly flat surface and antennas are assumed to be mostly perpendicular to the surface of the surveyed medium; for rough surveying surfaces with non-negligible topography, corrections must be carried out to accurately plot the location of reflections as seen in the radargram. The consequences of neglecting surface topography have been well discussed (Goodman, Nishimura, Hongo, & Higashi, 2006) (Dojack, 2012) (Zhang, Zhong, Li, & Zeng, 2014), and there are correction techniques built into popular processing programs like GPR-SLICE to automatically address these concerns.

For these surveys, a simple static correction was performed, as local 'topographic' roughness was on a small enough scale not to cause pitch and yaw of antennas. For each tarp position, horizontal and vertical lines of best fit were plotted through the middle of the tarp, and the direction normal to these lines was used as the projection direction for radargrams; in general the projection angle across tarps was an average of 52°. The 'topography' of the pillar face was accounted for by carrying out time-zero correction with a trace-by-trace routine. By projecting all tarps at a 52° angle and plotting horizontal lines for each tarp at similar locations, horizontal cross sections of the pillar at different heights are observed, as in Figure 2.10.

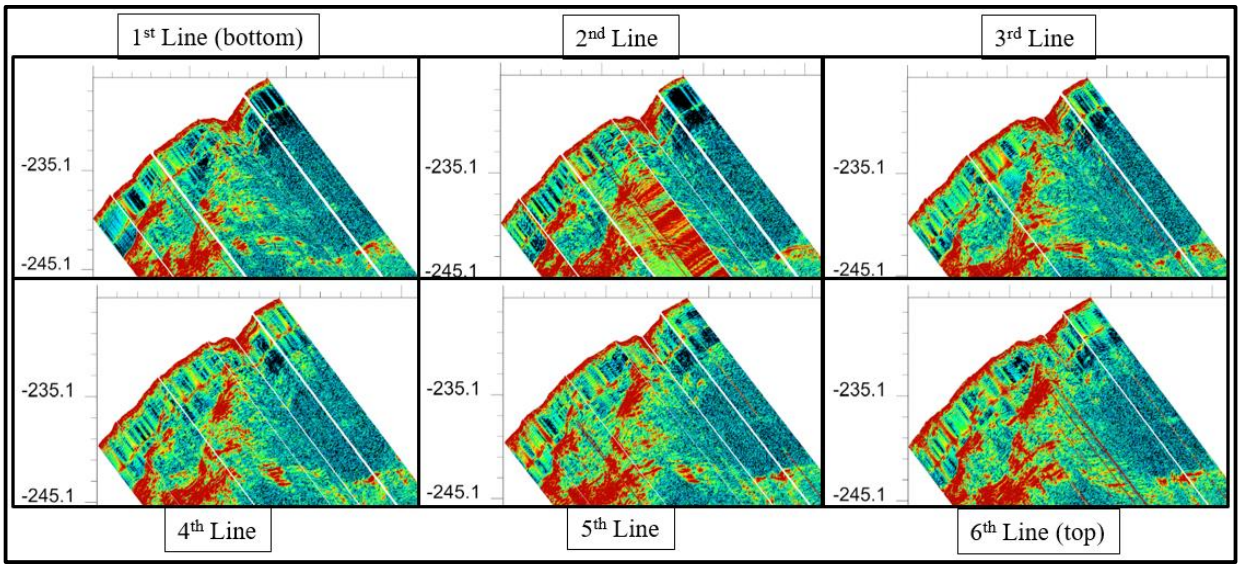

Figure 2.10 - Horizontal Cross Sections

3.2 Isosurface Generation and Mapping

While the true size and location of reflectors is not precise for Figure 2.10 as all tarps are projected at the same angle, noticeable changes can be seen developing in the 4th, 5th, and 6th horizontal lines compared to the 1st, 2nd, and 3rd lines. To better generalize each tarp grid, 35 interpolations were made between horizontal and vertical lines and then a 3D volume based on the processed data and interpolated data was compiled. A view of the 3D volume for Tarp A with some horizontal and vertical lines removed is seen in Figure 2.11.

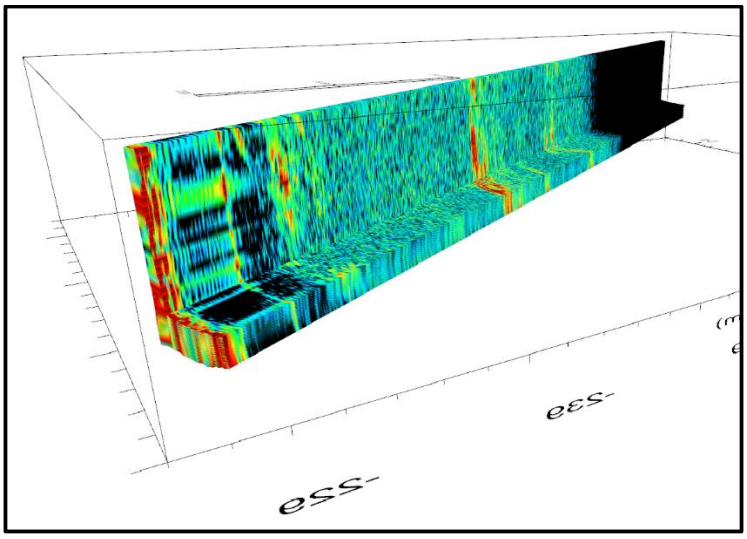

Figure 2.11 - 3D Volume from Interpolated Grid Lines; Some Horizontal and Vertical Lines Removed for Visibility

To extract reflection events from these volumes, it was useful to consider some threshold amplitude value to constitute a likely reflection. When this threshold was determined, it was then necessary to extract those reflection events above the threshold value as either points or isosurfaces. GPR-SLICE allows for automatic isosurface extraction based on a threshold value that can be expressed as a percentage of the highest amplitude signal within a dataset. For

instance, a 0% threshold would generate isosurfaces at all points within a data volume while an 80% threshold would generate isosurfaces only at reflection events with amplitudes that are 80% or more of the highest amplitude recorded in the volume. The rendering of these surfaces relies on the Marching Cubes algorithm (Goodman, GPR-SLICE_Software_Manual40495.pdf, 2019) (Anderson, 2019). Using a cutoff threshold of 75% for the volume in Figure 2.11 produces the isosurfaces seen in yellow in Figure 2.12.

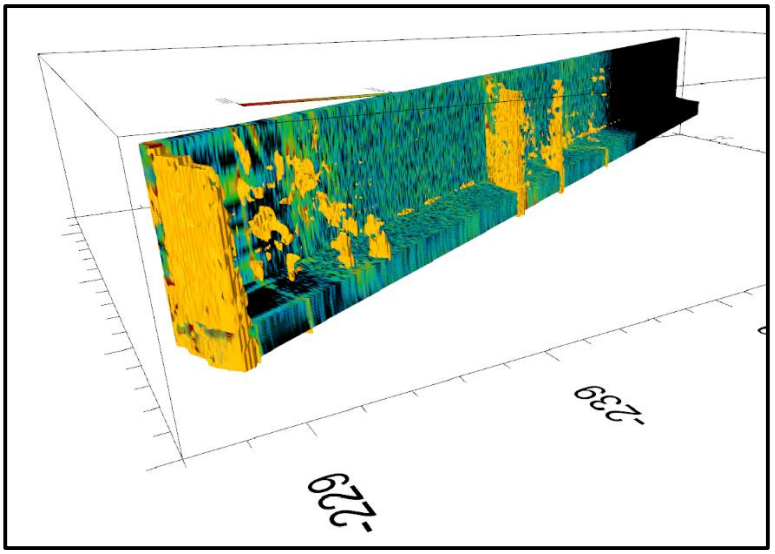

Figure 2.12 - 3D Volume with Isosurfaces [75%]

Using 75% as a first-pass threshold value for each tarp volume, the isosurfaces were exported as both mesh files and point files of vertices. In Rhinoceros 5.0, the point files of vertices were mapped with respect to the tarp surfaces and isosurface locations were compared to the pillar geometry. At this point, some noise from bad traces was filtered out manually, as bad traces tend to show repetitive high-amplitude 'ringing' signals throughout the depth of the radargram. These repetitive signals would satisfy the 75% threshold and appear in the isosurface files along with the useful surfaces. Once the noise was filtered, the surfaces from all of the tarp grids were plotted together to identify commonalities and surface trends, as seen in Figure 2.13.

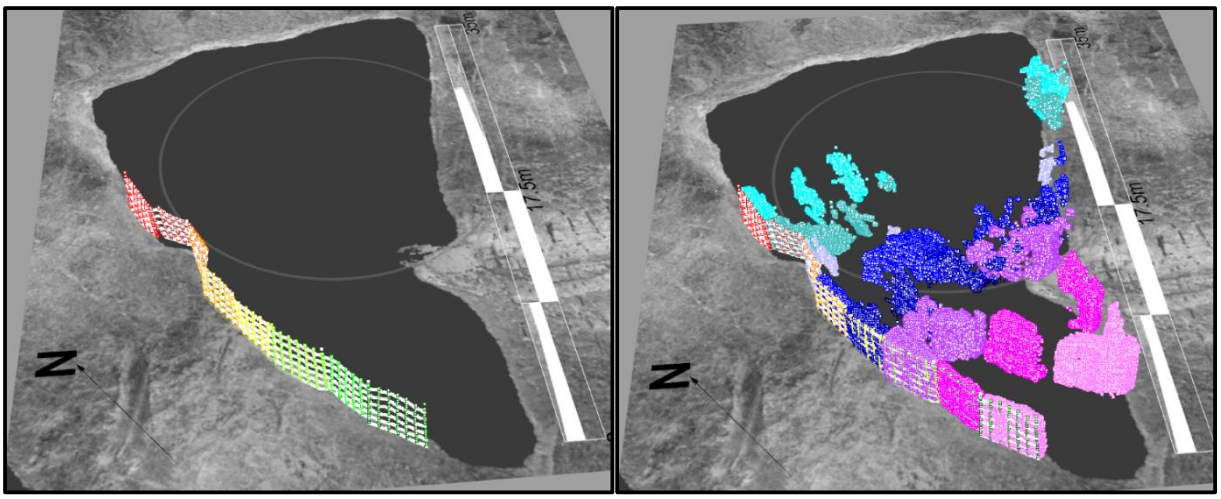

Figure 2.13 - Plotted Isosurface Vertex Points

Any isosurface points beyond the opposite edge of the pillar were also filtered out and considered likely to be processing noise and/or multiples. The pillar image seen in Figure 13 is a top-down view of a laser-scanned point cloud of the pillar; a single image was used for mapping due to the computational demand involved with manipulating millions of points. Encouragingly, when the filtered isosurface vertex points for each tarp grid were plotted with respect to the tarp shot locations, reflections at or nearly at the pillar boundary as seen in the laser-scan image were observed for each tarp grid. This implied that the projection angles used as simple static corrections for each tarp grid were likely adequate. A top-down view of the points in Figure 2.13 is seen in Figure 2.14.

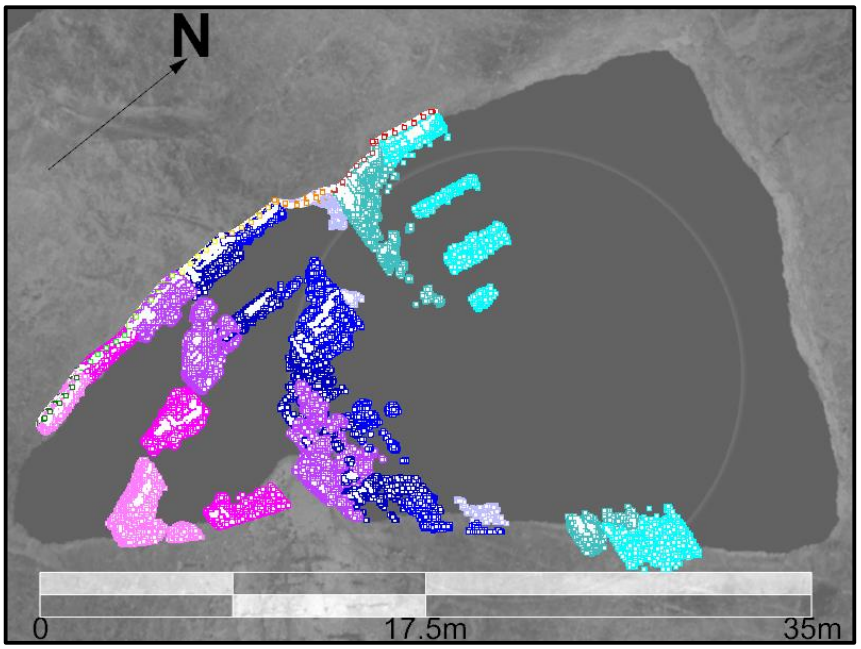

Figure 2.14 - Isosurface Vertex Points, Top-Down

The continuity among points between tarps observed in Figure 2.14 followed the expected trends based on previous 2D surveys of the pillar. The isosurface areas characterized by dense clusters of points likely indicated actual void volumes within the pillar; looking back at Figure 2.10, there were dense clusters of high amplitude signals that arose once the radar waves traveled beyond the pillar boundary and were traveling in air. These same clustering signatures were seen within the pillar at certain heights, and may have occurred as the radar waves refracted into a void space and then reflected between the sides of the void, causing multiple reflections at short delays from one another from the same reflector. Assuming that the dense clusters of points represented voids, the 'front' and 'back' of these clusters represented the surfaces of the probable voids. Meshing through the front and back of these clusters produced representative surfaces. These surfaces were generated from isosurface points by highlighting a thin layer of the 'front' and 'back' of the clusters and exporting these points to I-Site Studio 6.1, which has a complex surface generation from points function (Maptek, 2019). In this function, first a simple surface is generated as a reference, and from this reference a complex surface is generated which more closely fits all of the input points. A visual example of the two surfaces is seen in Figure 2.15.

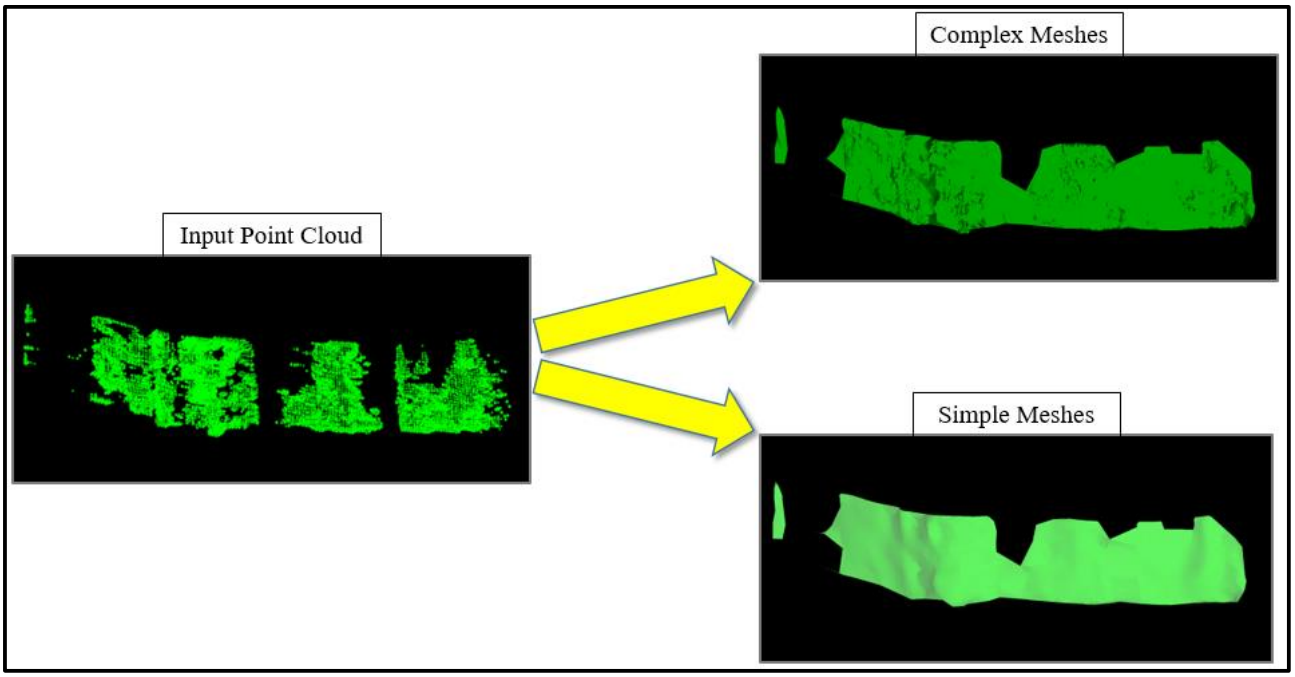

Figure 2.15 - Complex & Simple Surfaces from I-Site Studio 6.1

While the complex meshes more accurately represent the input point cloud, the simple meshes better represent the likely reflector surface in reality, smoother and more of an approximation compared to the jaggedness of the complex meshes. Once all of the surfaces had been generated for each of the identified clusters in the isosurface data, the surfaces were plotted, as seen in Figure 2.16.

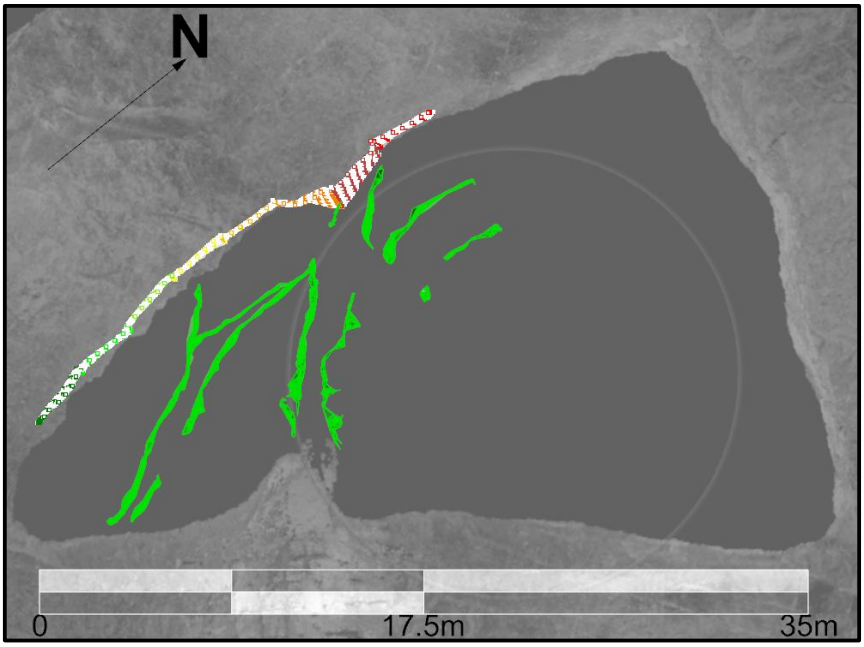

Figure 2.16 - Representative Meshes at Assumed Void Boundaries

The location of the voids based off of the representative surfaces in Figure 2.16 agreed well with the predicted karst void positioning in Figure 2.1. Adjusting the threshold value for isosurface generation was not tested, as the produced isosurfaces and subsequent representative void surfaces exceeded the researchers' expectations and agreed with the original predicted karst void shape/position. The isosurface reflections at the pillar boundaries were not characterized with representative surfaces.

4. Conclusions & Future Work

In this work, representative karst void surfaces at depths up to 20 meters were constructed from 3D GPR data. An artificial surveying surface (smooth tarp) was required to properly survey along pre-marked survey lines. LiDAR scans of shot locations were necessary to accurately record map files. The pillar boundaries were useful reference markers for mapping identified in the processed GPR radargrams, and such references would not be present in typical GPR surveys. Additional data may be used to confirm reflection positions, such as targeted drilling or borehole scoping.

The constructed karst void surfaces are useful indicators for mine engineers regarding the ultimate stability of the mine pillar. These surfaces may be imported into a numerical model during the geometrical design of the model, and their interaction with a discrete fracture network will comprehensively represent actual in-situ geological conditions. Additionally, karst features that are seen in common positions but different depths associated with mine tunnels in a multi-level layout can be extensively mapped and studied with this technique. These efforts would result in advantageous considerations for hydrogeological studies to identify sources of water intrusion into mine tunnels.

The logical 'next step' in verification of this methodology is to conduct a similar gridded 3D survey at an active face. For this style of geophysical surveying to be adopted practically by industry, its merits must be established and the time frame for data collection must fit into a cyclic production schedule without causing unnecessary delay. This case study achieved reliable results from these proposed surveying techniques, establishing the benefit of GPR as an aid to geotechnical studies. With the right equipment, software, and expertise, these methodologies can be simply and quickly employed in an underground room-and-pillar mining scheme.

5. References

Alija, S., Torrijo, F. J., & Qunita-Ferreira, M. (2013). Geological engineering problems associated with tunnel construction in karst rock masses: The case of Gaverres tunnel (Spain). *Engineering Geology*, 103-111.

Anderson, B. (2019, 4 17). *An Implementation of the Marching Cubes[1] Algorithm.* Retrieved from Carleton Edu: http://www.cs.carleton.edu/cs_comps/0405/shape/marching_cubes.html

Andriani, G. F., & Parise, M. (2017). Applying rock mass classifications to carbonate rocks for engineering purposes with a new approach using the rock engineering system. *Journal of Rock Mechanics and Geotechnical Engineering*, 364-369.

Annan, A. P. (2002). GPR - History, Trends, and Future Developments. *Subsurface Sensing Technologies and Applications*, 253-270.

Annan, A., & Davis, J. L. (1976). Impulse radar sounding in permafrost. *Radio Science*, 383-394.

Baggett, J. G., Abbasi, A., Monsalve, J., Bishop, R., Ripepi, N., & Hole, J. (2019). Ground Penetrating Radar for Karst Detection in Underground Stone Mines. *Mining, Metallurgy, and Exploration*.

Baggett, J., Abbasi, A., Monsalve, J., Bishop, R., Ripepi, N., & Hole, J. (2019). Ground Penetrating Radar for Karst Detection in Underground Stone Mines. *Mining, Metallurgy, and Exploration*.

Ballard, R. F., Cuenod, Y., & Jenni, J. P. (1982). Detection of karst cavities by geophysical methods. *Bulletin of Engineering Geology and the Environment*, 153-157.

Bin, L., Zhengyu, L., Shucai, L., Lichao, N., Maoxin, S., Huaifeng, S., . . . Yonghao, P. (2017). Comprehensive surface geophysical investigation of karst caves ahead of the tunnel face: A case study in the Xiaoheyan section of the water supply project from Songhua River, Jilin, China. *Journal of Applied Geophysics*, 37-49.

Bliss, J. D., Hayes, T. S., & Orris, G. J. (2008). *Limestone - A Crucial and Versatile Industrial Mineral Commodity.* Denver, CO: United States Geological Survey.

Davis, J., & Annan, A. P. (1989). Ground-Penetrating Radar For High-Resolution Mapping of Soil and Rock Stratigraphy. *Geophysical Prospecting*, 531-551.

Dojack, L. (2012). *Ground Penetrating Radar Theory, Data Collection, Processing, and Interpretation: A Guide for Archaeologists.* Vancouver: University of British Colombia.

Esterhuizen, G. S. (2007). *AN EVALUATION OF THE STRENGTH OF SLENDER PILLARS.* The National Institute of Occupational Safety & Health.

Esterhuizen, G. S., Dolinar, D. R., & Ellenberger, J. L. (2011). *Pillar strength in underground stone mines in the United States.* Pittsburgh, PA: The National Institute of Occupational Safety & Health.

Esterhuizen, G. S., Dolinar, D. R., Ellenberger, J. L., Prosser, L. J., & Iannacchione, A. T. (2007). *Roof Stability Issues in Underground Limestone Mines in the United States.* Pittsburgh: National Institute for Occupational Safety and Health.

Esterhuizen, G. S., Dolinar, D. R., Ellenberger, J. L., Prosser, L. J., & Iannacchione, A. T. (2012). *Roof Stability Issues in Underground Limestone Mines in the United States.* Pittsburgh, PA: NIOSH.

Goodman, D. (2019, 2 3). *GPR-SLICE_Software_Manual40495.pdf.* Retrieved from Gpr-Survey: https://www.gpr-survey.com/subscribers-only.html

Goodman, D., Nishimura, Y., Hongo, H., & Higashi, N. (2006). Correcting for Topography and the Tilt of Ground-penetrating Radar Antennae. *Archaeological Prospection*, 159-163.

GPR Systems & Surveying Equipment. (2019, April 5). Retrieved from Sensors & Software: https://www.sensoft.ca/gpr-products/

Grasmueck, M. (1996). 3-D ground-penetrating radar applied to fracture imaging in gneiss. *Geophysics*, 1050-1064.

Guo, Y., Xia, Y., Yang, X., Yang, M., Bai, H., & Feng, M. (2018). A comparative study of large karst cave point cloud registration in various scanning modes. *Survey Review*.

Guo, Z., Liu, D., Chen, Z., & Meng, H. (2012). Modeling on Ground Magnetic Anomaly Detection of Underground Ferromagnetic Metal Pipeline. *International Conference on Pipelines and Trenchless Technology.* China: National Natural Science Foundation of China.

Hasan, M. I., & Yazdani, N. (2016). An Experimental Study for Quantitative Estimation of Rebar. *Journal of Engineering*, 8.

Jacob, R. W., & Urban, T. M. (2016). Ground-Penetrating Radar Velocity Determination and Precision Estimates Using Common-Midpoint (CMP) Collection with Hand-Picking, Semblance Analysis and Cross-Correlation Analysis: A Case Study and Tutorial for Archaeologists. *Archaeometry*.

Kemeny, J., & Donovan, J. (2005). *Rock mass characterisation using LIDAR and automated point cloud processing.* Ground Engineering.

Kovin, O. N. (2010). *Ground penetrating radar investigations in Upper Kama potash mines.* Missouri S&T.

Kuniansky, E. L., Weary, D. J., & Kaufmann, J. E. (2016). The current status of mapping karst areas and availability of public sinkhole-risk resources in karst terrains of the United States. *Hydrogeology*, 613-624.

Leech, W. D., Jaoude, I. B., & Ghanem, N. (2008). *Madiq Tunnel, Lebanon: TBM Tunneling vs. Karst Geology.* Beirut.

Lorig, L. J., Darcel, C., Damjanac, B., Pierce, M., & Billaux, D. (2015). Application of discrete fracture networks in mining and civil geomechanics. *Mining Technology*, 239-254.

Mah, J. P. (2012). *Three-Dimensional Laser Imaging for Rock Mass Characterization.* Ottawa, Ontario: Carleton University.

Maptek. (2019, 4 17). *Maptek PointStudio*. Retrieved from Maptek Products: https://www.maptek.com/products/pointstudio/index.html

Monaghan, W. D., & Trevits, M. A. (2004). *Application of Ground Penetrating Radar to Evaluate the Extent of Polyurethane Grout Infiltration for Mine Roof Control.* Pittsburgh: NIOSH.

Monsalve, J. J., Baggett, J., Bishop, R., & Ripepi, N. (2017). Application of Laser Scanning for Rock Mass Characterization and Discrete Fracture Network Generation in an Underground Limestone Mine. *37th International Conference on Ground Control in Mining*, (pp. 183-192). Morgantown, WV.

Ozdemir, C., Demirci, S., Yigit, E., & Yilmaz, B. (2014). A Review on Migration Methods in B-Scan Ground Penetrating Radar Imaging. *Mathematical Problems in Engineering*, 16.

Parise, M., Gabrovsek, F., Kaufmann, G., & Ravbar, N. (2018). *Recent advances in karst research: from theory to fieldwork and applications.* London: Geological Society London.

Parise, M., Gabrovsek, F., Kaufmann, G., & Ravbar, N. (2018). *Recent advances in karst research: from theory to fieldwork and applications.* London: Geological Society of London.

Parkhomenko, E. I. (1967). *Eletrical Properties of Rocks.* Moscow, USSR: Institute of Physics of the Earth.

Riddle, G. I., Hickey, C. J., & Schmitt, D. R. (2007). *Subsurface Tunnel Detection Using Electrical Resistivity Tomography and Seismic Refraction Tomography: A Case Study.* Oxford, MS: National Center for Physical Acoustics.

Roberts, D., Tolfree, D., & McIntyre, H. (2007). Using confinement as a means to estimate pillar strength in a room and pillar mine. *Proceedings of the first Can-US rock mechanics symposium* (pp. 1455-61). London: Taylor & Francis.

Simmons, G. (1972). The surface electrical properties experiment. *Lunar Geophysics*, 258-271.

Slob, E., Sato, M., & Olhoeft, G. (2010). Surface and borehole ground-penetrating-radar developments. *Geophysics*, 103-120.

Software, S. &. (2019, April 11). *Noggin GPR Specifications*. Retrieved from Sensors & Software: https://www.sensoft.ca/products/noggin/specification/

Sweet, P. C. (1986). *Virginia's Lime Industry.* Charlottesville: Virginia Division of Mineral Resources.

Villaescusa, E. (1998). *Geotechnical design for dilution control in underground mining.* Kalgoorlie, Western Australia: Western Australia School of Mines.

Vrkljan, I. (2009). *Rock Engineering in Difficult Ground Conditions - Soft Rocks and Karsts.* London: CRC Press.

Wagner, H. (1992). Pillar design in South African collieries. *Proceedings of the workshop on coal pillar mechanics and design* (pp. 283-301). US Bureau of Mines.

Waltham, A. C., & Fookes, P. G. (2003). Engineering classification of karst ground conditions. *Quarterly Journal of Engineering Geology and Hydrogeology*, 101-118.

Wang, Y., Zhang, Z., Ren, Q., Wu, Y., & Peng, Z. (2012). Application of LTD-2100 Ground Penetrating Radar to Advanced Forecast in Diversion Tunnel of Jinping Hydroelectric Power Station. *14th International Conference on Ground Penetrating Radar* (pp. 57-61). Shanghai: IEEE.

Weidong, P., Fancheng, M., Renguo, G., Yonglei, L., & Zhengbo, H. (2012). Relationship Between Operation Technology of Ground Penetrating Radar and Precision of Advanced Forecast. *International Conference on Computer Science and Electronics Engineering* (pp. 640-644). IEEE.

Wiseman, J., & El-Baz, F. (2007). *Remote Sensing in Archaeology.* Boston, MA: Springer Science + Business Media, LLC.

Zhang, D., Zhong, R., Li, J., & Zeng, F. (2014). Topographic Correction of GPR Profiles Based on Laser Data. *35th International Symposium on Remote Sensing of Environment.* Beijing, China: IOP Publishing Ltd.

Chapter 3: A GROUND PENETRATING RADAR SURVEY OF A SILL PILLAR IN A MULTI-LEVEL STEEPLY DIPPING UNDERGROUND STONE MINE

Jonathan Baggett, Virginia Tech, Blacksburg, VA

Alexandra Menza, Virginia Tech, Blacksburg, VA

Dr. Nino Ripepi, Virginia Tech, Blacksburg, VA

Abstract

This work summarizes a campaign of ground penetrating radar surveys in a steeply dipping underground limestone mine to detect and map unknown geologic structures within sill pillars between mine levels. By identifying the structural conditions and any irregular voids in the sill pillar, roof instability in the tunnel below the sill pillar may be better addressed, and issues such as dilution and blast inefficiency may be mitigated when the sill pillar is eventually blasted to recover the ore. These efforts are motivated by the need to ensure mine worker's health and safety in these environments; this work is part of a NIOSH funded project for this purpose.

While borehole scoping and pattern drilling are traditional tools currently used to identify geologic, structural, and irregular conditions in tunnel roofs, these techniques offer inference limited to the holes in which they are applied, and interpolation between hole data is unavoidable. Additionally, previous studies on roof falls in underground stone mines are predominantly focused on relatively flat deposits. Ground penetrating radar (GPR) is a nondestructive geophysical method that is used to detect electrical interfaces in resistive mediums at depth. Due to the advantageous geometry for surveying at the case-study mine and the applicability of GPR in resistive rocks, this geophysical method was selected (Esterhuizen G. S., Dolinar, Ellenberger, Prosser, & Iannacchione, 2007).

1. Introduction

In all underground mining operations, much focus is emphasized on monitoring geologic conditions as mine tunnels are advanced. This monitoring is essential for excavation design, hazard detection, blast optimization, and maximizing economical ore recovery. Monitoring the geological, structural, hydrogeological, and irregular conditions of the roof is especially critical for preventing rock falls and designing roof bolting schemes. One hazardous condition that may also be encountered in limestone mining operations is the presence of karst voids; not only do these voids provide a free face for rock blocks, they often are formed along a hydrogeological network where preexisting discontinuities and other voids interact. Unfortunately, karst voids are spatially chaotic and difficult to predict ahead of tunneling without detailed hydrogeological and geologic studies of a rock mass. Due to the potential situation of karst voids and structural discontinuities interacting above the tunnel roof, ground control schemes in underground stone mines may need to be updated regularly based on changing ground conditions (Vrkljan, 2009; Parise, Gabrovsek, Kaufmann, & Ravbar, 2018; Villaescusa, 1998).

Additionally, in multi-level mines that initially leave sill pillars in place and later recover the ore via benching, karst features and discontinuities below the floors of tunnels may prove problematic when blast holes are drilled and fired. As a consequence of these hazards, blasts may be inefficient, previously stable sill pillars may be prone to instability as the benching stages are carried out, and significant dilution of recoverable ore may occur. Mining engineers traditionally make adjustments to blasting patterns based off of information collected by the drillers as production holes are drilled, however the usefulness and clarity of that information cannot always be guaranteed.

There are several geophysical methods that may be employed for mapping voids and irregularities in the subsurface, and these methods are well established for several industries. Methods include resistivity anomaly analyses, seismic refraction, magnetic resistance sensors, and others. GPR transmits radio waves at a set frequency into a medium, and these waves travel until they reflect at conductivity interfaces within the medium, such as an air-rock interface, a water-rock interface, or a clay-rock interface. The two-way travel time of the radar waves is measured and converted to depth using the velocity of the radar waves within the medium. As limestone is predominantly resistive, the case-study mine is free of clay seams, and the necessary depth-of-penetration was within 10 meters, GPR was the ideal geophysical method for this campaign (Guo, Liu, Chen, & Meng, 2012) (Riddle, Hickey, & Schmitt, 2007).

2. Methodology

2.1 Case Study Mine

The case-study mine resides in a synclinal Ordovician limestone which has been subjected to regional thrusting and hosts an interconnected system of karst void reservoirs. The orebody dips at approximately 30° towards southeast as visible from the outcrop and portal but flattens to approximately 18° in the deeper levels of the mine where GPR surveying was conducted, about halfway between the mine entrance and the bottom of the mine. The mine is multilevel, with levels connected by a spiral ramp which also acts as the primary escape-way. Each level has an east and west section branching off of the spiral ramp; at present, each branch contains a footwall and hanging wall tunnel separated by 24 meter square pillars, and tunnels are approximately 8.5 meters tall and 14 meters wide. Figure 3.1 shows a sketched cross section of the orebody with the mine plan superimposed, as well as a plan view of an east branch on one mine level (Sweet, 1986).

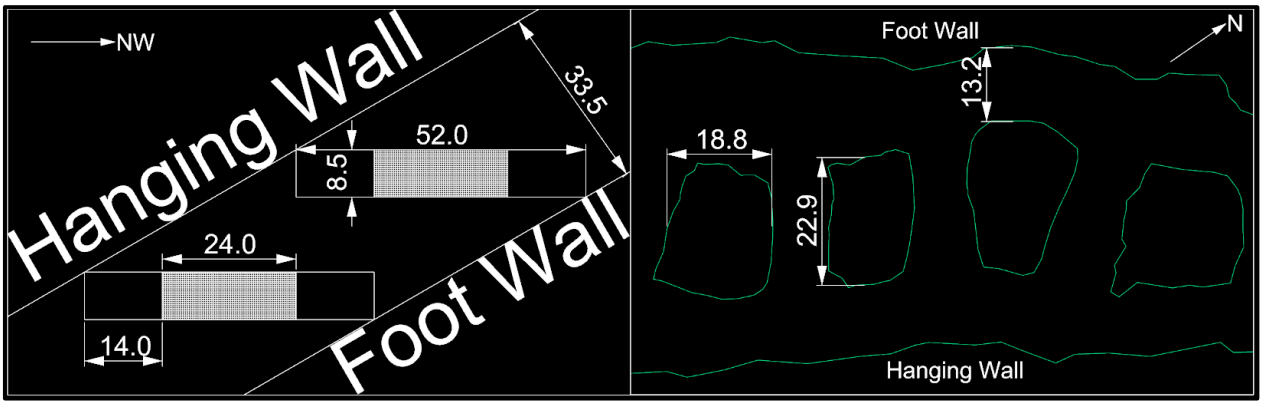

Figure 3.1 - Mine Plan Sketch and Plan View

Figure 3.1 shows that sequential tunnels will be positioned so that the footwall tunnel of a deeper level is directly beneath the hanging wall tunnel of the next shallowest tunnel; the volume of rock between these tunnels forms a sill pillar approximately 8.5 to 11 meters thick. According to the mining plan, once the overlapping mine tunnels have reached their furthest extents, the sill pillar is stoped via several blasts to recover the ore. Along with the predominant joint sets naturally occurring in the sill pillar, there may be inconspicuous voids between the mine tunnels that could potentially effect blast design, blast efficiency, and the stability of pillar walls in the fully stoped entry.

In a previous work (Monsalve, Baggett, Bishop, & Ripepi, 2017), karst void formation along a predominant joint set within the orebody was described. The voids are typically vertically planar, aligned almost North to South (255°), and are thus encountered roughly perpendicular to the mine tunnels. The size of voids ranges from miniscule to massive such that one void may be continuous through several mine levels. Figures 3.2 and 3.3 show a point cloud obtained via LiDAR of an upper and a lower mine level; points highlighted in red represent visually identified karst voids. The voids seen in these figures are relatively narrow and pose minimal risk for roof fall, whereas expansive and large voids found within the mine require extensive ground

control support; some tunnels have been abandoned due to massive karst features above the tunnel that simply cannot be controlled via feasible measures.

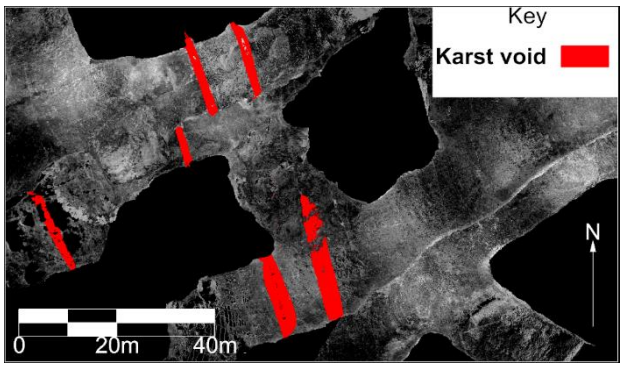

Figure 3.2 - Top Down View of Karst Voids through 2 Mine Levels

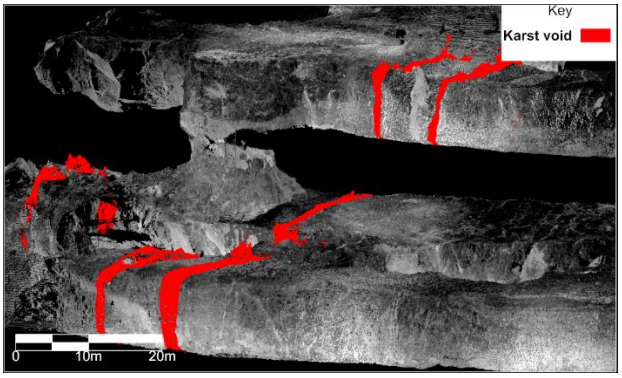

Figure 3.3 - Isometric View of Karst Voids through Two Mine Levels

While mapping the continuation of a karst void seen on an upper level into a lower level may offer inference into the size and position of the karst void within the sill pillar, this prediction can only be confirmed with supporting data, such as GPR reflections.

2.2 Terravision Surveying Underground

A series of sill pillar GPR surveys in the tunnels seen in Figure 3.3 were conducted using a cart-based system called the Terravision, originally produced by Underground Imaging Technologies. The Terravision contains a 1.55-meter-wide antenna bank with 14 pairs of 400 MHz central frequency bistatic GPR antennas. The antenna bank is housed in an aluminum frame for towing and there is a control unit also connected to the frame through which survey parameters are adjusted manually and data acquisition is performed. Two flat-free wheels were needed on each side of the unit to adequately traverse the rough mine tunnel roadways. The Terravision is pictured in Figure 3.4.

Primarily designed for utility mapping in near-surface applications, the Terravision and its companion software collect 2D data for each of the 14 antenna pairs and then interpolate between them to create a 3D volume of GPR reflection data. The system can collect data while being towed at a maximum speed of 8 kilmoeters per hour; with a width of 1.55 meters and an approximate depth-of-penetration of 4.5 meters, the Terravision is capable of collecting roughly 950 cubic meters of GPR data per minute.

GPR surveying was planned in mine tunnels that had significant sill pillar surface area (as adjustments are made to the mine plan, this may change) as well as visible karst voids that have a mapped continuation between mine levels. Depth-of-penetration of radar waves depends on input power, wavelength (frequency), level of attenuation within the medium (energy loss), and proper surveying techniques; based off of previous works, depth-of-penetration for this rock mass was expected to be great enough to possibly image reflections off of the rock-air interface (roof) of the tunnel below the survey. Three mine levels that at present are being actively developed were identified as candidates for surveying based off of the previously stated criteria, and a plan view of these tunnels is seen in Figure 3.5 (Baggett J. , et al., 2019).

Figure 3.4 - The Terravision

Figure 3.5 - Plan View of GPR Candidate Tunnels

Corresponding to labels in Figure 3.5, surveys in the upper and middle elevation levels were conducted primarily in the highlighted areas of overlap. Survey swaths are as wide as the antenna bank (1.55 meters) and 30 meters long. Additional surveys in karst feature zones beyond the sill pillar overlap areas were performed. A survey map is included in Figure 3.6; areas of the tunnel with standing water present in the floor had to be avoided, as radar energy is completely attenuated by water and

the sill pillar beneath could not be surveyed. Line 9 in the higher elevation tunnel was cut short at 15 meters due to mechanical problems with towing, however the data represented is accurately mapped.

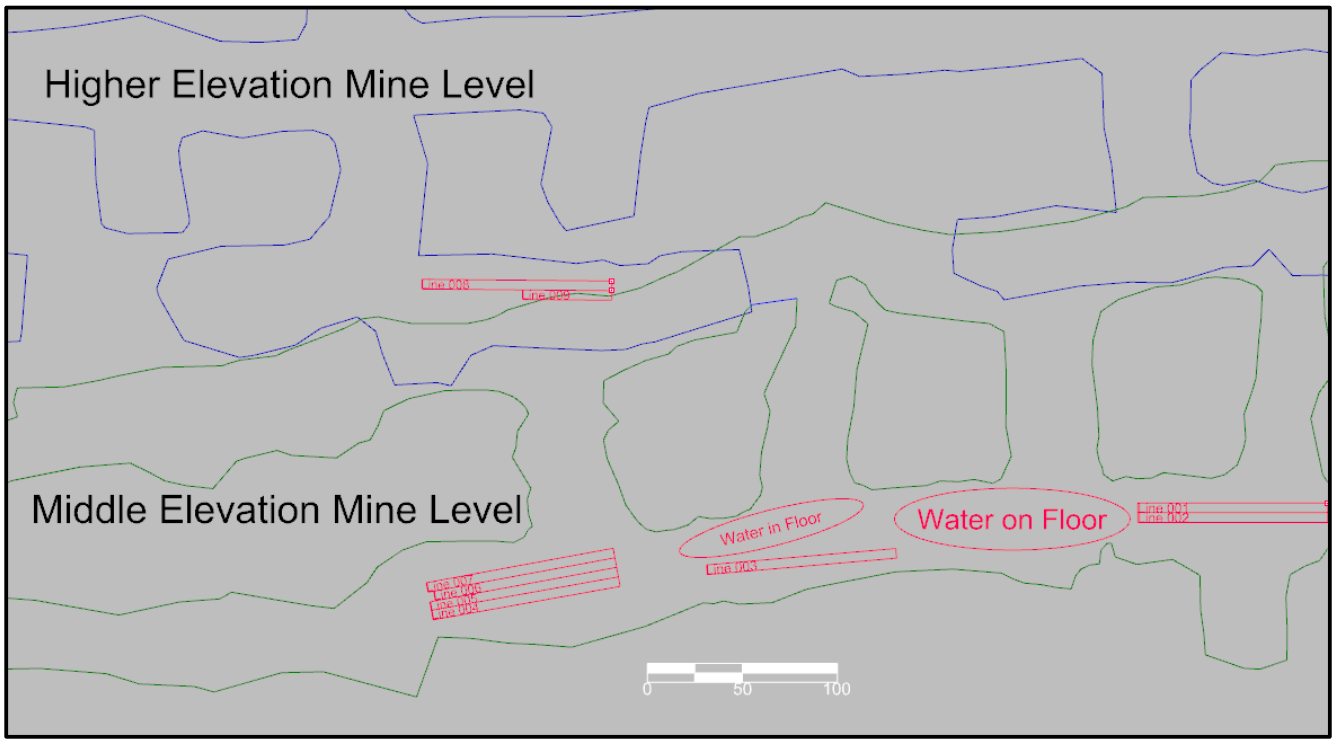

Figure 3.6 - Map of Surveys

As the cart is towed, an odometer triggers the transmitting antenna and a 'shot' is fired. For this surveying campaign, a diesel powered UTV was ideal for towing and surveys were performed by one to three people. Based off of previous works (Baggett J. , et al., 2019) and published values (Jacob & Urban, 2016), the estimated radar velocity through the limestone is approximately 0.11 meters per nanosecond, about a third of the speed of light (0.3 m/ns). The travel time of radar waves from the transmitting antenna to the reflector in the sill pillar and back to the receiving antenna is converted to depth using the estimated velocity. In total, nine survey swaths were performed between the higher and middle elevation levels, seven of which were on the middle elevation level.

2.3 Data Processing

Data processing begins by constructing a map file for each survey swath which details the start and end XY coordinates of the Terravision. The 'topography' of the surveyed surface must also be accounted for and corrected; while the tunnel roadways' roughness had an impact on the Terravision's wheels, the floor was mostly flat and elevation change was considered negligible. The raw data is then loaded in RADAN, a well-known GPR processing program from GSSI. In RADAN, the processing flow is constructed and applied to correct for unavoidable surveying consequences such as travel time of the radar wave in air and energy attenuation at depth, among other things. The flow for this surveying campaign is:

1. Time-zero correction
2. Bandpass filters
3. Signal Gain

While the Terravision antenna bank is mostly coupled to the ground surface during surveying, air gaps are encountered as the two surfaces are not perfectly parallel. For this reason, the radar waves travel in air for some short time and some energy reflects off of the ground surface while some energy is transferred into the floor; this short time contains no useful data, and is therefore subtracted out via the time-zero correction. The time-zero corrections also corrects for the system time delay before the receiving antenna begins recording reflections As the sill pillar is not purely homogenous isotropic limestone, some inhomogeneities in the rock scatter radar waves and produce signals outside of the frequency band transmitted by the Terravision. These signals are filtered out with the bandpass filtering operation. Finally, to amplify the deeper reflections in the rock mass that have traveled farther and thus lost more energy during attenuation and due to spherical spreading, a gain curve is applied to the bandpass filtered data. As reflectors were expected to be predominantly planar and continuous, antenna spacing was negligible, and reflector depth was relatively shallow, migration was not used for this dataset. A view of the raw data and fully processed data in RADAN is seen in Figure 3.7; reflections have been highlighted (Ozdemir, Demirci, Yigit, & Yilmaz, 2014).

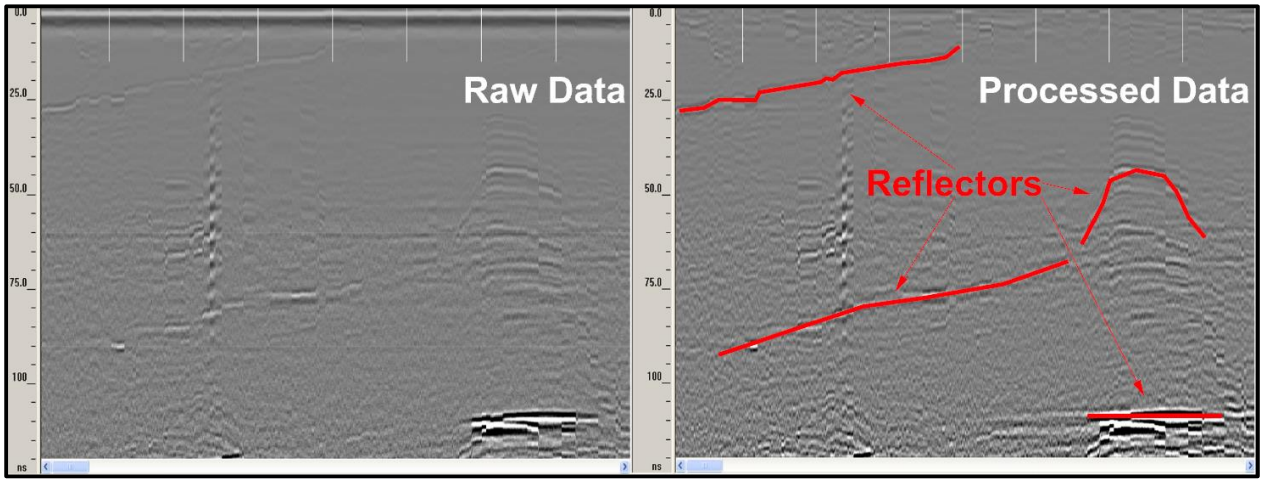

Figure 3.7 - Raw Data and Processed Data, RADAN

Once processed completely in RADAN, reflection data is opened in the Terravision's companion software, customized for interpretation. This software displays the processed radargrams in a 3D space as well as the interpolations between each radargram. The software is primarily used for mapping, analyzing, and detecting reflection surfaces from various viewing angles. Corresponding to the map of surveys in Figure 3.6, a map of the data is seen in Figure 3.8.

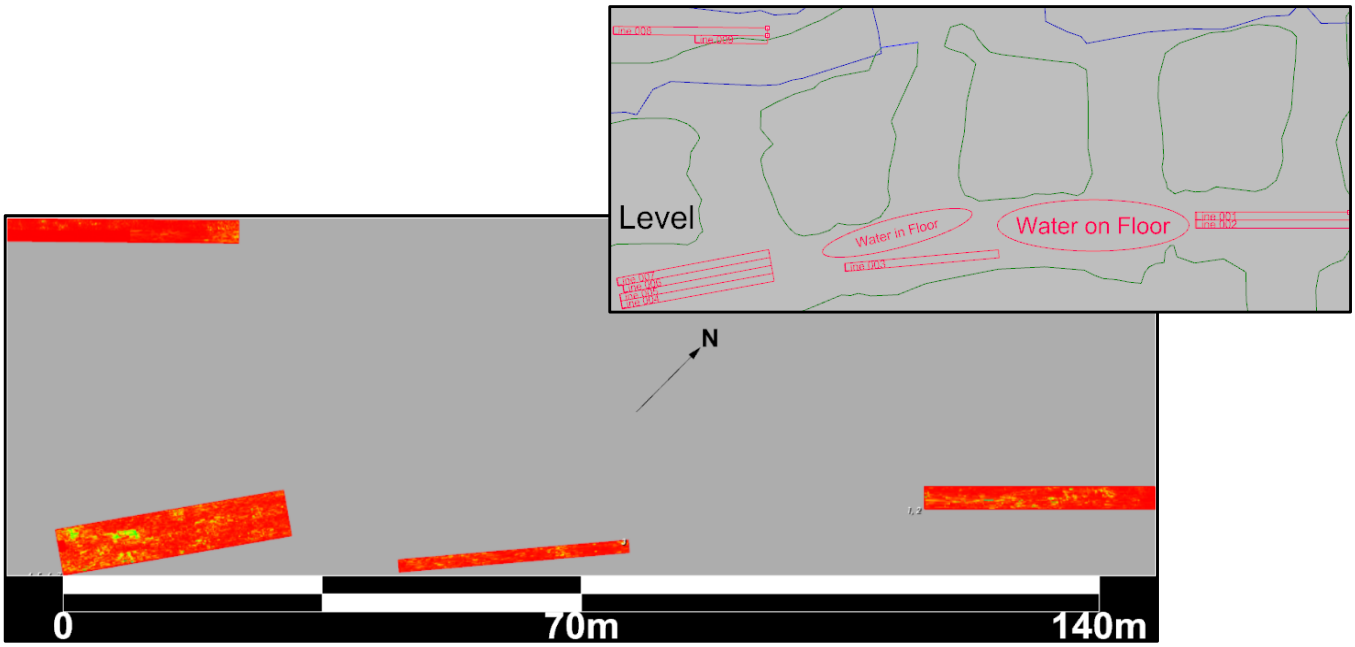

Figure 3.8 – Fully Processed Data in Custom Interpretation Software; Plan View

Cross sections of these radar swaths show the true nature of reflections at depth, and the custom software allows for cross sections at any parallel, perpendicular, or oblique angle to the survey direction to be queried as the entire dataset is interpolated. Additionally, horizontal cross sections through the data volumes may be viewed at any depth down to the bottom of the dataset. Parallel and perpendicular cross sections can be seen in Figure 3.9.

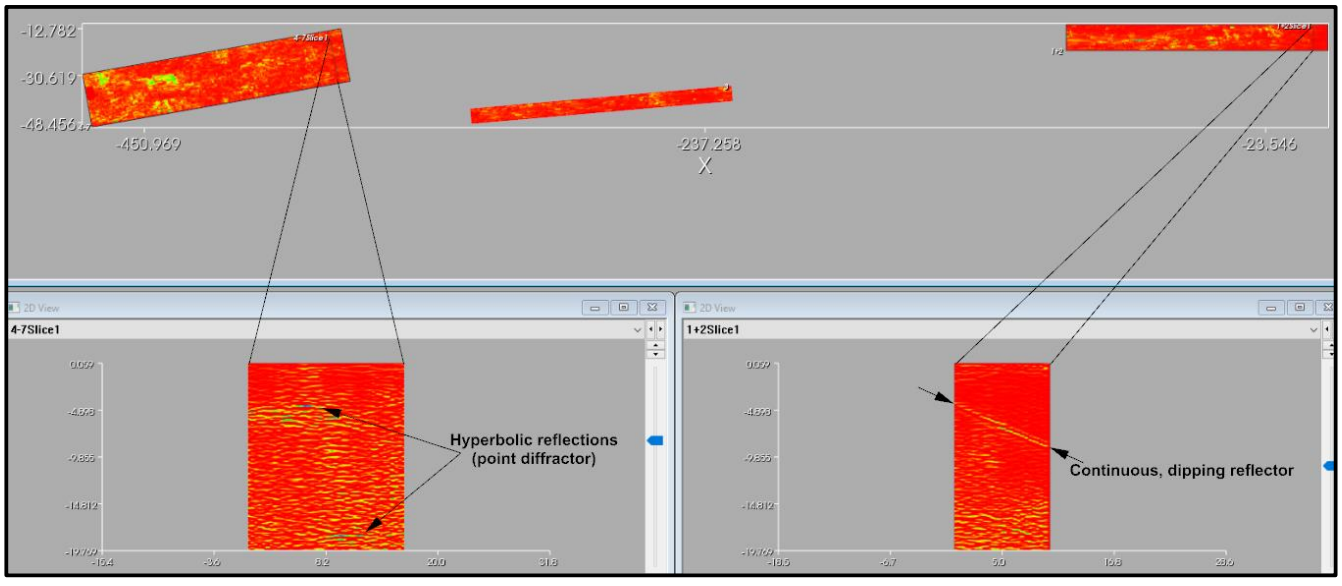

Figure 3.9 - Parallel and Perpendicular Cross Sections

In the custom interpretation software, a point picking tool allows the user to place representative nodes along visible reflection surfaces; these nodes retain XYZ coordinates that correspond to the cross section position and the depth of the reflector as seen in the cross section. To characterize reflection surfaces in this work, first a cross section perpendicular to the

surveying direction at the east extent of a radar swath was queried and points along any visible reflectors were picked. A second perpendicular cross section 5 scans towards the west was then queried, and the picking process was repeated iteratively, moving forward 5 scans at a time. Next, a cross section parallel to the survey direction was queried at the south-east extent of the radar swath and nodes were drawn along reflector surfaces. The parallel cross sections were moved forward 3 scans at a time iteratively, as to best characterize the narrow 1.55-meter width of the swath. Once the entire volume had been analyzed parallel and perpendicular and several thousand nodes had been given XYZ coordinates, the nodes were then exported as a comma-separated-value file to be imported into mapping software.

As the mapped nodes represent reflecting geologic anomalies in a 3D space, they are better represented by surfaces. The nodes with apparent relations to one another, such as several nodes forming a dipping plane or hyperbola were then meshed together to create representative reflection surfaces. Meshes are useful for interpolating between points, but are limited in applicability due to the chaotic variation of karst features. While a set of interpolated surfaces may not be the most accurate way to represent a karst void, this method is the most logical way to represent features seen in this dataset and processed using the software tools employed in this campaign. The picked nodes from one swath and the meshes generated through those points may be seen in Figure 3.10.

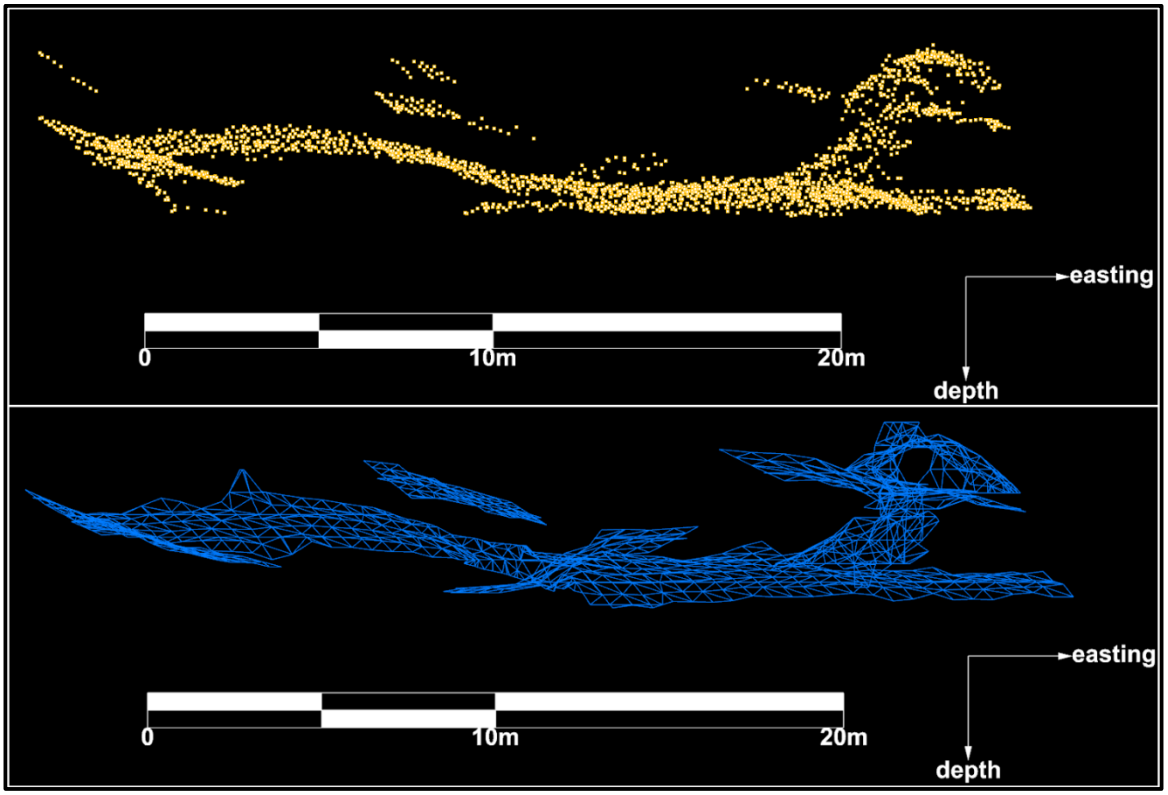

Figure 3.10 - Picked Nodes and Representative Meshes

For mapping, LiDAR scans of each of the three overlapping tunnels were performed to create a 3D point cloud of the survey space, as seen in Figures 3.2 and 3.3. I-Site Studio 6.1 from Maptek was used to display these point clouds. The representative reflection meshes from the custom interpretation software were imported into I-Site to view reflections with respect to the tunnel geometries. A view of the reflection surfaces analyzed from the first two radar swaths mapped with respect to the tunnel point clouds is shown in Figure 3.11. Due to the water in the tunnel floor, the swaths in this section end just before passing over / under the karst void. Figures 3.12, 3.13, and 3.14 show the other reflection sections.

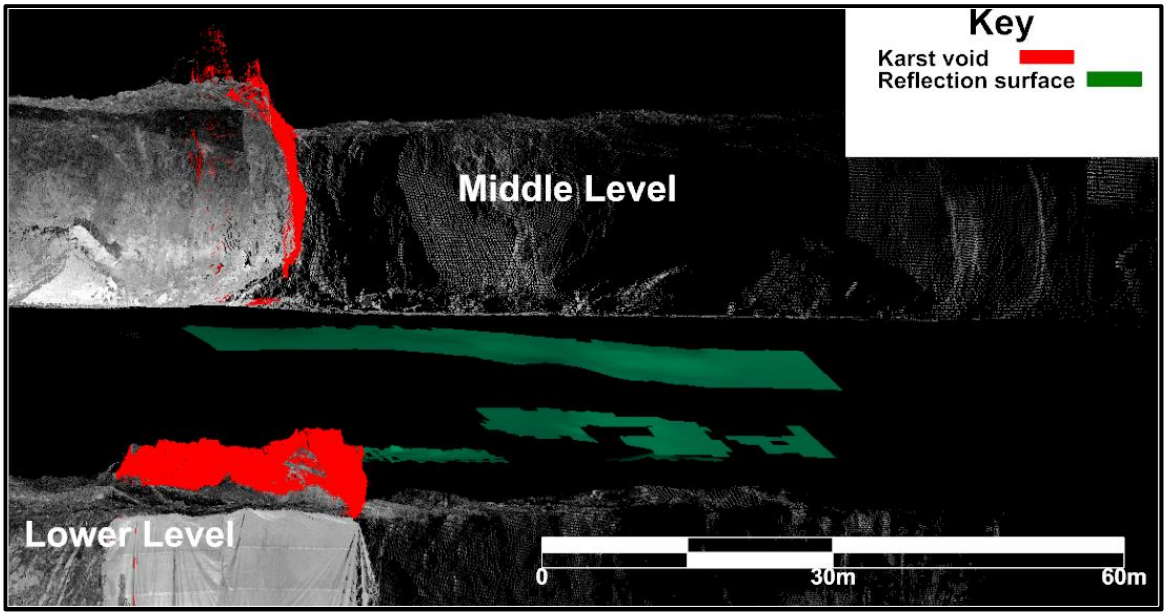

Figure 3.11 - Section 1, Reflection Surfaces

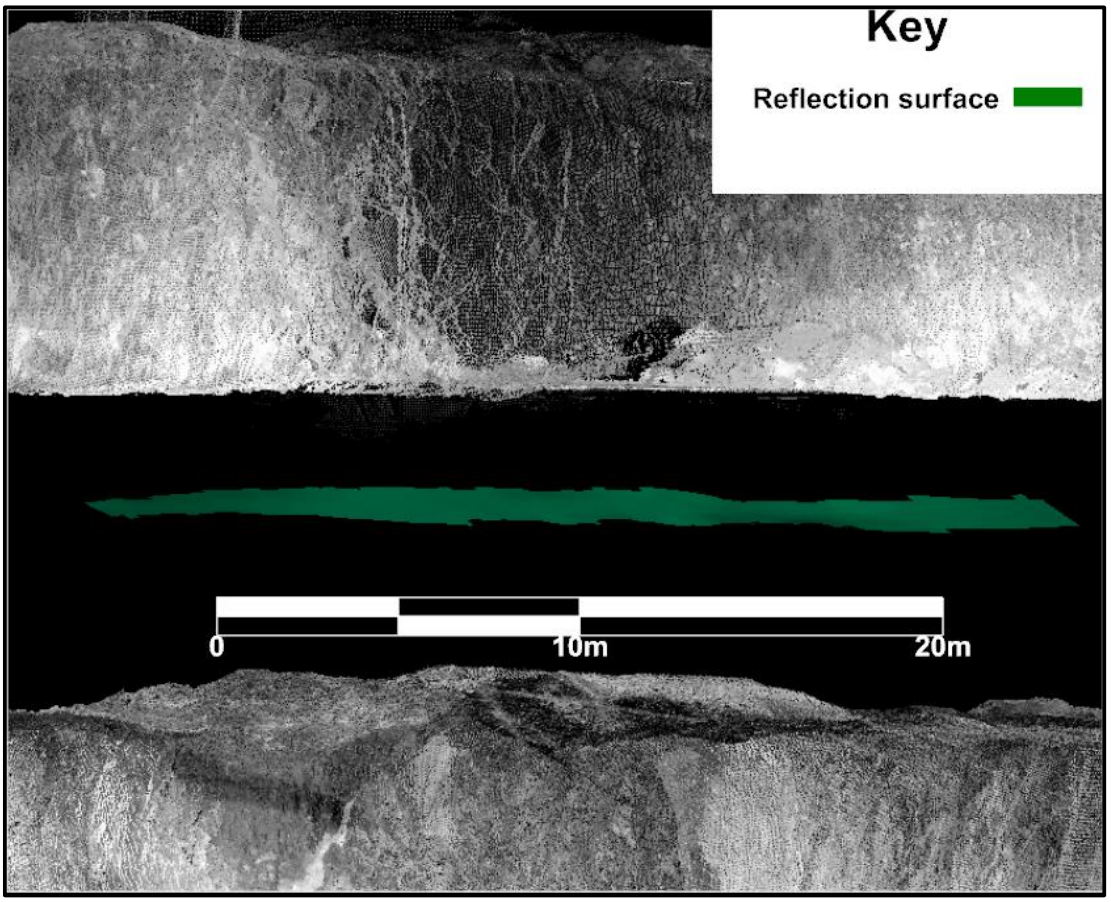

Figure 3.12 - Section 2, Reflection Surfaces

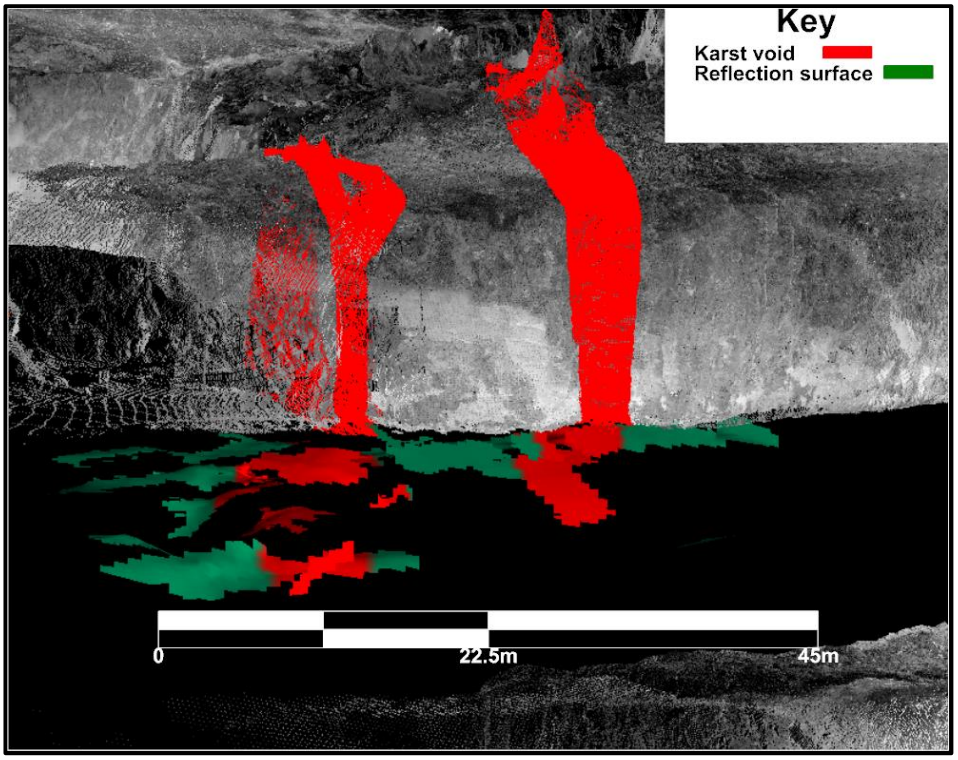

Figure 3.13 - Section 3, Reflection Surfaces

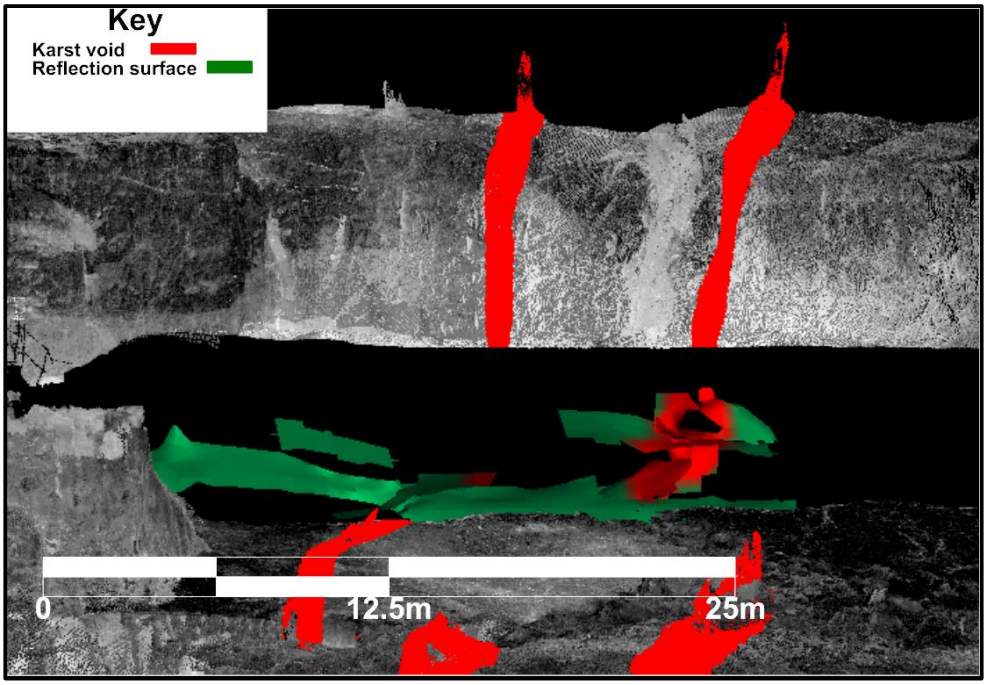

Figure 3.14 - Section 4, Reflection Surfaces

In Figures 3.11 and 3.12, or Section 1 and Section 2, a continuous reflector dipping in the same direction as the dip of the orebody is pictured. Neither Section 1 nor Section 2 include reflections from karst voids, however the same continuous dipping reflector is seen in both sections. In Figures 3.13 and 3.14, or Section 3 and Section 4, both a continuous dipping reflector and karst void reflections are seen, however it should be noted that Section 3 is a view of the middle elevation tunnel while Section 4 is a view of the highest elevation tunnel.

3. Results and Discussion

3.1 Continuous Dipping Reflector Analysis

Within I-Site Studio 6.1, the strike and dip of points or planes may be analyzed. This function proves useful when analyzing the continuous dipping reflector. Areas of the visible reflector in each section were queried to best characterize the strike and dip of the mesh as generated from data processing. View of queried reflector areas are seen in Figure 3.15 for each section. Sixteen areas were queried on the continuous dipping reflector seen in all four sections.

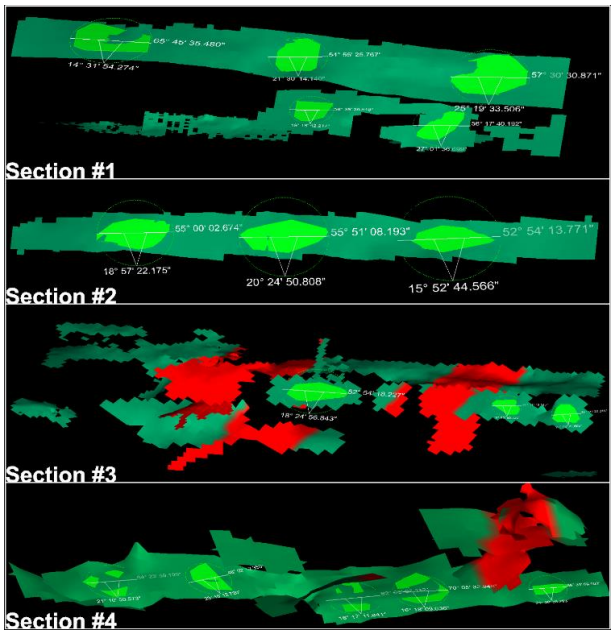

Figure 3.15 - Analyzing Strike and Dip of GPR Reflector

The process of querying dipping areas was repeated on the laser scanned point clouds of the mine tunnels where the bedding plane was visible. The dip of the GPR data reflecting surface was in the range of 15° to 22°, approximately the known dip of the bedding plane at this depth of the mine. Views of the queried bedding plane areas in all three tunnels is seen in Figure 3.16. In total, 33 areas on the bedding planes were queried for strike and dip. A stereonet summarizing the GPR reflection surface and one to summarize the visible bedding plane are seen in Figures 3.17 and 3.18 respectively. Table 3.1 summarizes the values of strike and dip for each.

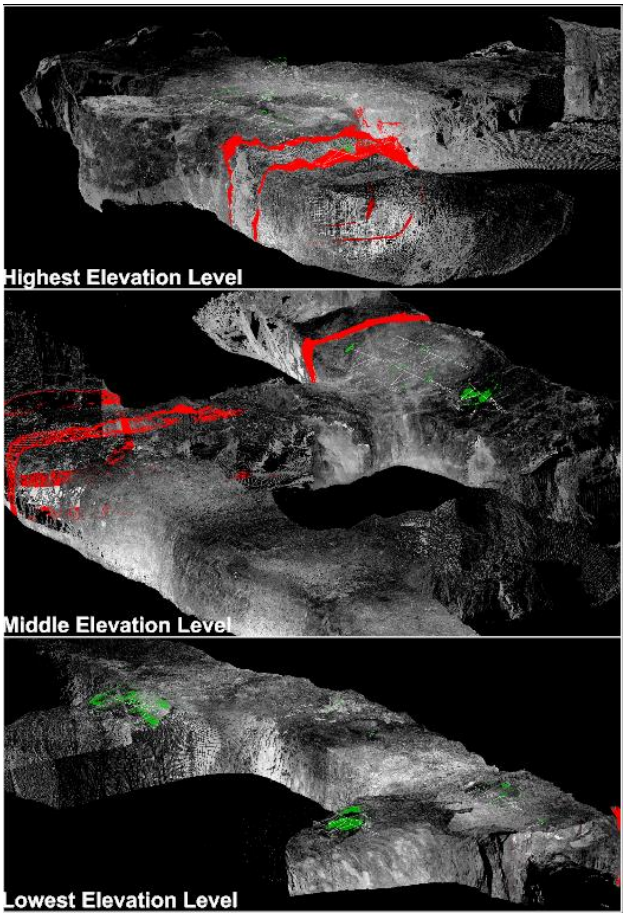

Figure 3.16 - Bedding Plane Strike and Dip

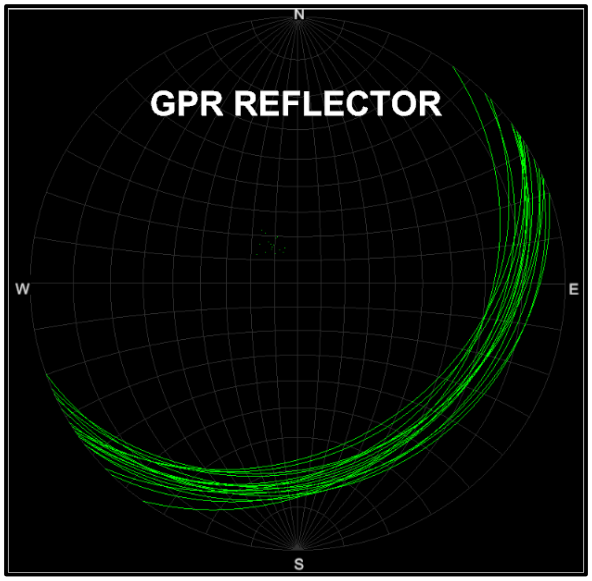

Figure 3.17 – Stereonet of Continuous, Dipping Reflection Surface

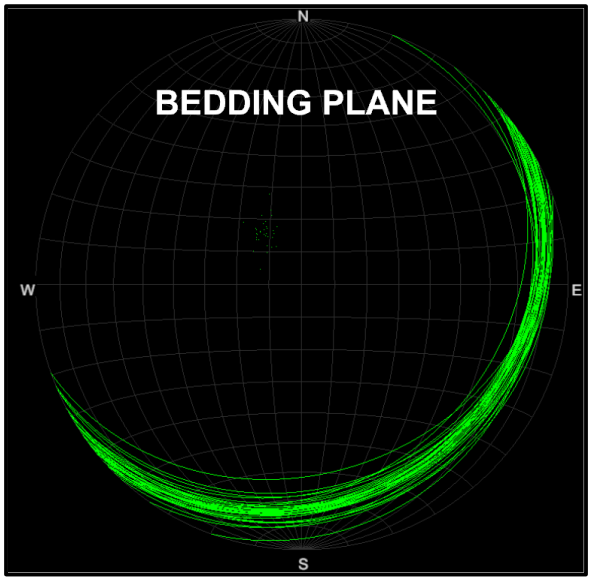

Figure 3.18 - Stereonet of Visible Bedding Plane

Table 3.1 - Strike and Dip of Reflection Surface and Bedding Plane

	Bedding Plane	GPR Reflector	% Difference
Dip (°)	19.7	19.8	0.6%
Strike (°)	54.1	55.8	3.0%
# of Queries	33	16	

From the similarity in strike and dip of the continuous dipping reflector and the visible bedding plane, it is concluded that reflections were in fact coming from spaced discontinuity surfaces in the sill pillar that are part of the bedding plane characteristic family. Furthermore, inspecting this dipping reflector in Section 4 indicates that this reflection was at the same depth as the roof of the middle elevation tunnel, which was not the case for all the other Sections. A closer look is seen in Figure 3.19.

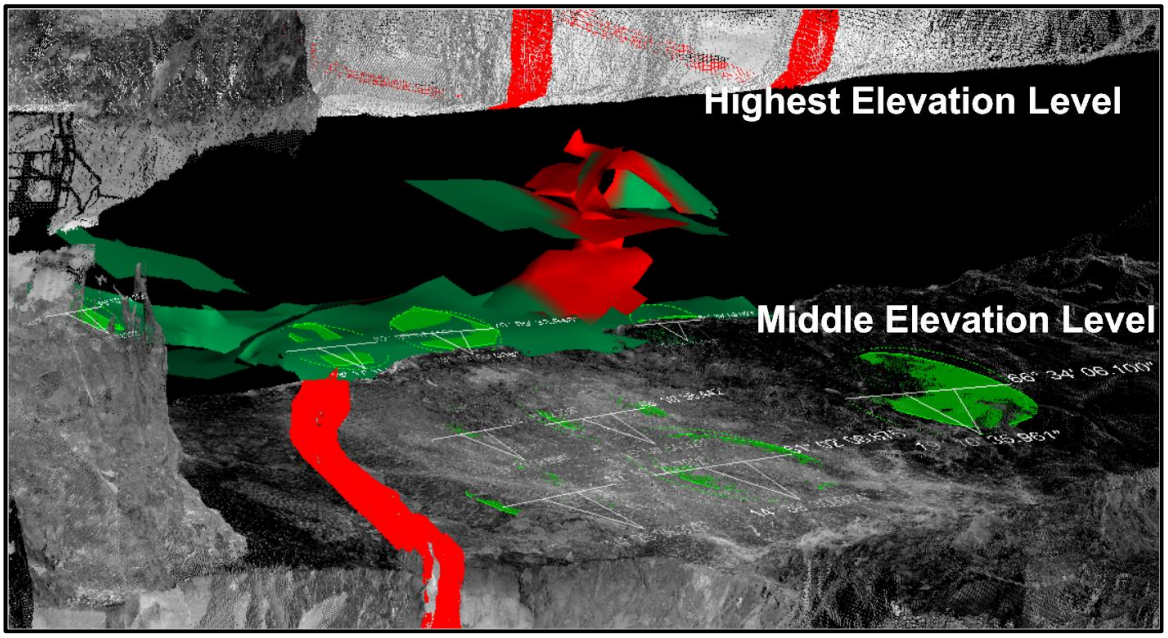

Figure 3.19 - Section 4 Closer Look

3.2 Karst Feature Reflection Analysis

Interpretation of karst feature reflections is not straightforward, as the karst void surface is not perpendicularly planar to the travel direction of the radar energy. On the contrary, the radar waves travel nearly parallel to the generalized 'plane' of most karst voids in this mine. With this limitation in mind, the karst feature reflections seen in Figures 3.13 and 3.14 (Section 3 and 4, respectively) require discussion. In Section 3, irregular reflections are detected at positions coinciding with the highlighted voids seen in the tunnel roof. The irregular signals extend down to the extents of the useful GPR data in these swaths, and there seems to be interaction with the bedding plane reflector. Of the two karst void positions, the left karst void in Figure 3.13 shows more irregularity, with several strong signals appearing in small clusters at depth around the karst void position. There is no clear indication of size or shape of the karst feature from these clusters, however their presence may indicate void apertures throughout the sill pillar ranging as deep as the useful GPR data.

In Section 4, in which two open karst voids are visible in the roof, reflections from the right void were clearly visible and pronounced, while there were no reflections whatsoever beneath the left void. In fact, the continuous dipping reflector below the left void was clearly imaged much deeper in the sill pillar, below where hypothetical karst feature reflections would be expected. The karst feature reflections that were imaged beneath the right void show a clear vertical profile beginning at the bottom of the GPR data and extending more than halfway through the sill pillar. Because the surface's shape is still irregular (and the GPR data is unmigrated), detailed conclusions regarding the shape and size of the karst feature are limited, however its aperture and depth can be assumed from the surfaces pictured in Figures 3.14 and 3.19.

If the generalized plane of these karst voids was perpendicular to the travel direction of the radar waves, there would be significantly greater surface area for waves to reflect off of, and that desirable geometry has been achieved in similar surveying campaigns in a previous work. Figure 3.20 shows an example of the consequences of survey geometry (Baggett J. , et al., 2019).

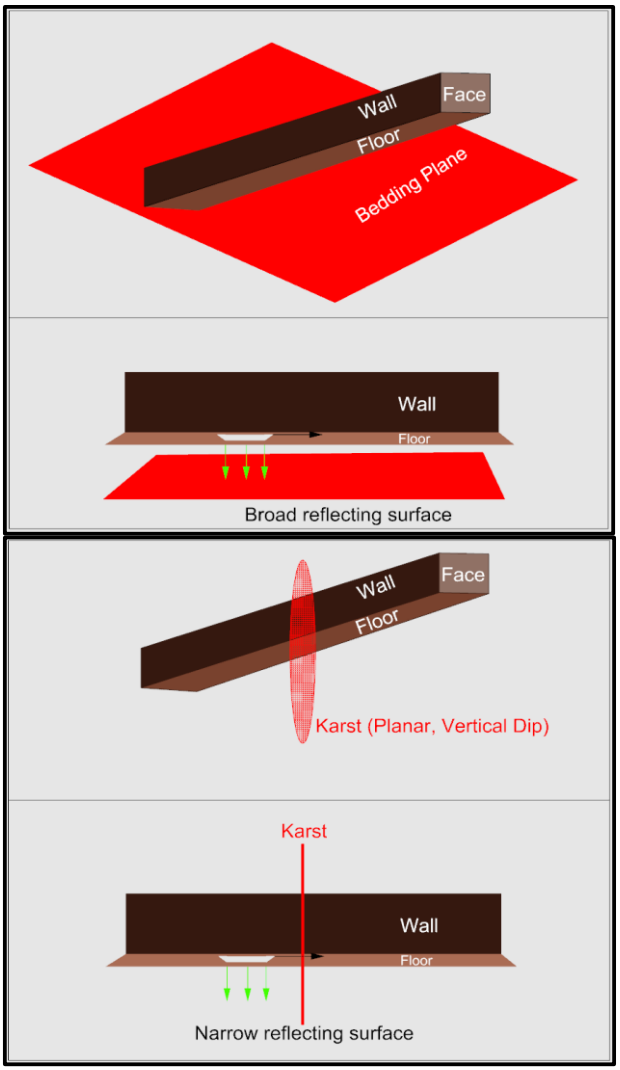

Figure 3.20 - Survey Geometry Consequence

4. Conclusions

In this GPR surveying campaign, discontinuities and karst voids hidden in the sill pillar between levels in a dipping limestone room-and-pillar mine were successfully imaged and mapped. The high resolution of data and large area surveyed would not have been attainable with traditional methods of geologic prediction. Reflection data for the karst voids offers limited implications due to the undesirable karst geometry, however assumptions regarding the aperture and extent of the karst feature at depth can be made. The Terravision GPR cart, operating at a central frequency of 400 MHz, was able to image radar wave reflections off of the calcite-filled bedding plane discontinuities that have apertures no larger than 2 millimeters, as confirmed by local investigations.

The results of this study may inform future endeavors for similar surveys, and the reflection data in this work serves as design inputs for sill pillar benching for mine personnel. Furthermore, the mapped void-discontinuity interactions may be used as inputs for numerical models to evaluate the stability of the lower tunnel roof and the sill

pillar as a rock unit. Additional data may be used to confirm reflection positions, such as targeted drilling or borehole scoping.

5. Acknowledgements

The authors would like to acknowledge NIOSH for funding this project, Dr. David Hanson of NIOSH for orchestrating Virginia Tech's use of the Terravision and for training the authors for field work and software analysis. Also, the authors acknowledge the personnel of the case-study mine for their support and participation in this research.

6. References

Alija, S., Torrijo, F. J., & Qunita-Ferreira, M. (2013). Geological engineering problems associated with tunnel construction in karst rock masses: The case of Gaverres tunnel (Spain). *Engineering Geology*, 103-111.

Anderson, B. (2019, 4 17). *An Implementation of the Marching Cubes[1] Algorithm.* Retrieved from Carleton Edu: http://www.cs.carleton.edu/cs_comps/0405/shape/marching_cubes.html

Andriani, G. F., & Parise, M. (2017). Applying rock mass classifications to carbonate rocks for engineering purposes with a new approach using the rock engineering system. *Journal of Rock Mechanics and Geotechnical Engineering*, 364-369.

Annan, A. P. (2002). GPR - History, Trends, and Future Developments. *Subsurface Sensing Technologies and Applications*, 253-270.

Annan, A., & Davis, J. L. (1976). Impulse radar sounding in permafrost. *Radio Science*, 383-394.

Baggett, J. G., Abbasi, A., Monsalve, J., Bishop, R., Ripepi, N., & Hole, J. (2019). Ground Penetrating Radar for Karst Detection in Underground Stone Mines. *Mining, Metallurgy, and Exploration*.

Baggett, J., Abbasi, A., Monsalve, J., Bishop, R., Ripepi, N., & Hole, J. (2019). Ground Penetrating Radar for Karst Detection in Underground Stone Mines. *Mining, Metallurgy, and Exploration*.

Ballard, R. F., Cuenod, Y., & Jenni, J. P. (1982). Detection of karst cavities by geophysical methods. *Bulletin of Engineering Geology and the Environment*, 153-157.

Bin, L., Zhengyu, L., Shucai, L., Lichao, N., Maoxin, S., Huaifeng, S., . . . Yonghao, P. (2017). Comprehensive surface geophysical investigation of karst caves ahead of the tunnel face: A case study in the Xiaoheyan section of the water supply project from Songhua River, Jilin, China. *Journal of Applied Geophysics*, 37-49.

Bliss, J. D., Hayes, T. S., & Orris, G. J. (2008). *Limestone - A Crucial and Versatile Industrial Mineral Commodity.* Denver, CO: United States Geological Survey.

Davis, J., & Annan, A. P. (1989). Ground-Penetrating Radar For High-Resolution Mapping of Soil and Rock Stratigraphy. *Geophysical Prospecting*, 531-551.

Dojack, L. (2012). *Ground Penetrating Radar Theory, Data Collection, Processing, and Interpretation: A Guide for Archaeologists.* Vancouver: University of British Colombia.

Esterhuizen, G. S. (2007). *AN EVALUATION OF THE STRENGTH OF SLENDER PILLARS.* The National Institute of Occupational Safety & Health.

Esterhuizen, G. S., Dolinar, D. R., & Ellenberger, J. L. (2011). *Pillar strength in underground stone mines in the United States.* Pittsburgh, PA: The National Institute of Occupational Safety & Health.

Esterhuizen, G. S., Dolinar, D. R., Ellenberger, J. L., Prosser, L. J., & Iannacchione, A. T. (2007). *Roof Stability Issues in Underground Limestone Mines in the United States.* Pittsburgh: National Institute for Occupational Safety and Health.

Esterhuizen, G. S., Dolinar, D. R., Ellenberger, J. L., Prosser, L. J., & Iannacchione, A. T. (2012). *Roof Stability Issues in Underground Limestone Mines in the United States.* Pittsburgh, PA: NIOSH.

Goodman, D. (2019, 2 3). *GPR-SLICE_Software_Manual40495.pdf.* Retrieved from Gpr-Survey: https://www.gpr-survey.com/subscribers-only.html

Goodman, D., Nishimura, Y., Hongo, H., & Higashi, N. (2006). Correcting for Topography and the Tilt of Ground-penetrating Radar Antennae. *Archaeological Prospection*, 159-163.

GPR Systems & Surveying Equipment. (2019, April 5). Retrieved from Sensors & Software: https://www.sensoft.ca/gpr-products/

Grasmueck, M. (1996). 3-D ground-penetrating radar applied to fracture imaging in gneiss. *Geophysics*, 1050-1064.

Guo, Y., Xia, Y., Yang, X., Yang, M., Bai, H., & Feng, M. (2018). A comparative study of large karst cave point cloud registration in various scanning modes. *Survey Review*.

Guo, Z., Liu, D., Chen, Z., & Meng, H. (2012). Modeling on Ground Magnetic Anomaly Detection of Underground Ferromagnetic Metal Pipeline. *International Conference on Pipelines and Trenchless Technology.* China: National Natural Science Foundation of China.

Hasan, M. I., & Yazdani, N. (2016). An Experimental Study for Quantitative Estimation of Rebar. *Journal of Engineering*, 8.

Jacob, R. W., & Urban, T. M. (2016). Ground-Penetrating Radar Velocity Determination and Precision Estimates Using Common-Midpoint (CMP) Collection with Hand-Picking, Semblance Analysis and Cross-Correlation Analysis: A Case Study and Tutorial for Archaeologists. *Archaeometry*.

Kemeny, J., & Donovan, J. (2005). *Rock mass characterisation using LIDAR and automated point cloud processing.* Ground Engineering.

Kovin, O. N. (2010). *Ground penetrating radar investigations in Upper Kama potash mines.* Missouri S&T.

Kuniansky, E. L., Weary, D. J., & Kaufmann, J. E. (2016). The current status of mapping karst areas and availability of public sinkhole-risk resources in karst terrains of the United States. *Hydrogeology*, 613-624.

Leech, W. D., Jaoude, I. B., & Ghanem, N. (2008). *Madiq Tunnel, Lebanon: TBM Tunneling vs. Karst Geology.* Beirut.

Lorig, L. J., Darcel, C., Damjanac, B., Pierce, M., & Billaux, D. (2015). Application of discrete fracture networks in mining and civil geomechanics. *Mining Technology*, 239-254.

Mah, J. P. (2012). *Three-Dimensional Laser Imaging for Rock Mass Characterization.* Ottawa, Ontario: Carleton University.

Maptek. (2019, 4 17). *Maptek PointStudio*. Retrieved from Maptek Products: https://www.maptek.com/products/pointstudio/index.html

Monaghan, W. D., & Trevits, M. A. (2004). *Application of Ground Penetrating Radar to Evaluate the Extent of Polyurethane Grout Infiltration for Mine Roof Control.* Pittsburgh: NIOSH.

Monsalve, J. J., Baggett, J., Bishop, R., & Ripepi, N. (2017). Application of Laser Scanning for Rock Mass Characterization and Discrete Fracture Network Generation in an Underground Limestone Mine. *37th International Conference on Ground Control in Mining*, (pp. 183-192). Morgantown, WV.

Ozdemir, C., Demirci, S., Yigit, E., & Yilmaz, B. (2014). A Review on Migration Methods in B-Scan Ground Penetrating Radar Imaging. *Mathematical Problems in Engineering*, 16.

Parise, M., Gabrovsek, F., Kaufmann, G., & Ravbar, N. (2018). *Recent advances in karst research: from theory to fieldwork and applications.* London: Geological Society London.

Parise, M., Gabrovsek, F., Kaufmann, G., & Ravbar, N. (2018). *Recent advances in karst research: from theory to fieldwork and applications.* London: Geological Society of London.

Parkhomenko, E. I. (1967). *Eletrical Properties of Rocks.* Moscow, USSR: Institute of Physics of the Earth.

Riddle, G. I., Hickey, C. J., & Schmitt, D. R. (2007). *Subsurface Tunnel Detection Using Electrical Resistivity Tomography and Seismic Refraction Tomography: A Case Study.* Oxford, MS: National Center for Physical Acoustics.

Roberts, D., Tolfree, D., & McIntyre, H. (2007). Using confinement as a means to estimate pillar strength in a room and pillar mine. *Proceedings of the first Can-US rock mechanics symposium* (pp. 1455-61). London: Taylor & Francis.

Simmons, G. (1972). The surface electrical properties experiment. *Lunar Geophysics*, 258-271.

Slob, E., Sato, M., & Olhoeft, G. (2010). Surface and borehole ground-penetrating-radar developments. *Geophysics*, 103-120.

Software, S. &. (2019, April 11). *Noggin GPR Specifications*. Retrieved from Sensors & Software: https://www.sensoft.ca/products/noggin/specification/

Sweet, P. C. (1986). *Virginia's Lime Industry.* Charlottesville: Virginia Division of Mineral Resources.

Villaescusa, E. (1998). *Geotechnical design for dilution control in underground mining.* Kalgoorlie, Western Australia: Western Australia School of Mines.

Vrkljan, I. (2009). *Rock Engineering in Difficult Ground Conditions - Soft Rocks and Karsts.* London: CRC Press.

Wagner, H. (1992). Pillar design in South African collieries. *Proceedings of the workshop on coal pillar mechanics and design* (pp. 283-301). US Bureau of Mines.

Waltham, A. C., & Fookes, P. G. (2003). Engineering classification of karst ground conditions. *Quarterly Journal of Engineering Geology and Hydrogeology*, 101-118.

Wang, Y., Zhang, Z., Ren, Q., Wu, Y., & Peng, Z. (2012). Application of LTD-2100 Ground Penetrating Radar to Advanced Forecast in Diversion Tunnel of Jinping Hydroelectric Power Station. *14th International Conference on Ground Penetrating Radar* (pp. 57-61). Shanghai: IEEE.

Weidong, P., Fancheng, M., Renguo, G., Yonglei, L., & Zhengbo, H. (2012). Relationship Between Operation Technology of Ground Penetrating Radar and Precision of Advanced Forecast. *International Conference on Computer Science and Electronics Engineering* (pp. 640-644). IEEE.

Wiseman, J., & El-Baz, F. (2007). *Remote Sensing in Archaeology.* Boston, MA: Springer Science + Business Media, LLC.

Zhang, D., Zhong, R., Li, J., & Zeng, F. (2014). Topographic Correction of GPR Profiles Based on Laser Data. *35th International Symposium on Remote Sensing of Environment.* Beijing, China: IOP Publishing Ltd.

Chapter 4: Summary of Conclusions, Recommendations, Future Works

Karst voids may present ground control risks and hazards associated with water and caving material. The chaotic spatial randomness of karst void formation is a challenge for detecting, mapping, and predicting the size of voids. In this work, ground penetrating radar has been shown to detect karst features within a limestone pillar at depth, and the processed data offers inferences into the locations where these karst features expand into a large open void. The 2D reflection survey has limitations in describing how the karst features are oriented at different heights within the pillar, therefore multiple surveys are needed to properly describe the karst features in 3D. While some resolution in the reflected radar waves is not imaged with lower frequency surveys, the strong dielectric boundary between the limestone pillar and the karst void was clearly visible in the 200 MHz and 250 MHz data at depth.

In the 3D surveys, representative karst feature surfaces at depths up to 20 meters were constructed from GPR data. An artificial surveying surface (smooth tarp) was required to properly survey along pre-marked survey lines. LiDAR scans of shot locations were necessary to accurately record map files. The pillar boundaries were useful reference markers for mapping identified in the processed GPR radargrams, and such references would not be present in typical GPR surveys.

The constructed karst void surfaces are useful indicators for mine engineers regarding the ultimate stability of the mine pillar. These surfaces may be imported into a numerical model during the geometrical design of the model, and their interaction with a discrete fracture network will comprehensively represent actual in-situ geological conditions. Additionally, karst features that are seen in common positions but different depths associated with mine tunnels in a multi-level layout can be extensively mapped and studied with this technique. These efforts would result in advantageous considerations for hydrogeological studies to identify sources of water intrusion into mine tunnels.

In the Terravision surveying campaign, discontinuities and karst voids hidden in the sill pillar between levels in a dipping limestone room-and-pillar mine were successfully imaged and mapped. The high resolution of data and large area surveyed would not have been attainable with traditional methods of geologic prediction. Reflection data for the karst voids offers limited implications due to the undesirable karst feature geometry, however assumptions regarding the aperture and extent of the karst void at depth can be made. The Terravision GPR cart, operating at a central frequency of 400 MHz, was able to image radar wave reflections off of the calcite-filled bedding plane discontinuities that have apertures no larger than 2 millimeters, as confirmed by local investigations.

Other applications of GPR in underground stone mines include mapping thickness of strata in the immediate roof, investigating for faults in suspected areas, or even measuring thickness of the orebody layer in the floor with high frequency antennas. Similar pillar investigations may be conducted as a precursor to pillar strength estimations also.

Surveying campaigns in the future that follow similar survey design, surveying methodology, and processing flows may encounter different results depending on site geology, antenna specifications, and map file inputs. GPR is a useful investigation method, however its application is limited to predominantly resistant mediums with low moisture and negligible presence of clay seams. This implies that other geophysical methods would be better suited for metal mines and mines with considerable water intrusion. Fortunately, methods such as resistivity and seismic reflection are well established for mining exploration, and seismic reflection specifically has terminology mostly analogous to that for GPR.

The logical ‘next step’ following this research would be a 3D GPR survey on an active face in a tunnel to predict anomalies ahead of mining. Through conversations with members of industry and fellow researchers, the research team believes that an active face survey would be the most beneficial and practical use of GPR within this industry; it is our belief that the studies detailed in this work serve as proof of concept guidelines for such surveys.